อินเดียมอาร์เซไนด์ควอนตัมดอตโมเลกุลบนเทมเพลตนาโนโฮล/ลายตาราง

นายนิทัศน์ นคเรศไอศูรย์

บทคัดย่อและแฟ้มข้อมูลฉบับเต็มของวิทยานิพนธ์ตั้งแต่ปีการศึกษา 2554 ที่ให้บริการในคลังปัญญาจุฬาฯ (CUIR)
เป็นแฟ้มข้อมูลของนิสิตเจ้าของวิทยานิพนธ์ ที่ส่งผ่านทางบัณฑิตวิทยาลัย
The abstract and full text of theses from the academic year 2011 in Chulalongkorn University Intellectual Repository (CUIR)
are the thesis authors' files submitted through the University Graduate School.

วิทยานิพนธ์นี้เป็นส่วนหนึ่งของการศึกษาตามหลักสูตรปริญญาวิศวกรรมศาสตรมหาบัณฑิต
สาขาวิชาวิศวกรรมไฟฟ้า ภาควิชาวิศวกรรมไฟฟ้า
คณะวิศวกรรมศาสตร์ จุฬาลงกรณ์มหาวิทยาลัย
ปีการศึกษา 2558

ลิขสิทธิ์ของจุฬาลงกรณ์มหาวิทยาลัย

InAs quantum dot molecules on nanohole/cross-hatch pattern templates

Mr. Nitas Nakareseisoon

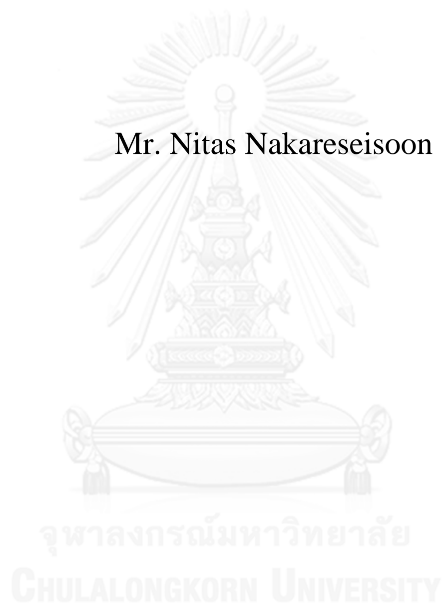

A Thesis Submitted in Partial Fulfillment of the Requirements
for the Degree of Master of Engineering Program in Electrical Engineering
Department of Electrical Engineering
Faculty of Engineering
Chulalongkorn University
Academic Year 2015

Copyright of Chulalongkorn University

Thesis Title	InAs quantum dot molecules on nanohole/cross-hatch pattern templates
By	Mr. Nitas Nakareseisoon
Field of Study	Electrical Engineering
Thesis Advisor	Associate Professor Dr. Songphol Kanjanachuchai

Accepted by the Faculty of Engineering, Chulalongkorn University in Partial Fulfillment of the Requirements for the Master's Degree

....Dean of the Faculty of Engineering
(Professor Dr. Bundhit Eua-arporn)

THESIS COMMITTEE

....Chairman
(Professor Dr. Somsak Panyakaew)

....Thesis Advisor
(Associate Professor Dr. Songphol Kanjanachuchai)

....External Examiner
(Dr. Noppadon Nuntawong)

จุฬาลงกรณ์มหาวิทยาลัย
Chulalongkorn University

นิทัศน์ นคเรศไอศูรย์ : อินเดียมอาร์เซไนด์ควอนตัมดอตโมเลกุลบนเทมเพลตนาโนโฮล/ลายตาราง (InAs quantum dot molecules on nanohole/cross-hatch pattern templates) อ.ที่ปรึกษาวิทยานิพนธ์หลัก: รศ. ดร. ทรงพล กาญจนชูชัย, 54 หน้า.

วิทยานิพนธ์ฉบับนี้ศึกษาวิวัฒนาการและลักษณะเฉพาะของควอนตัมดอตโมเลกุล (quantum dot molecules, QDMs) บนพื้นผิวลายตาราง (cross hatch patterns, CHPs) QDMs ถูกปลูกด้วยเทคนิคการกลบด้วยชั้นบางและปลูกซ้ำบนแผ่นฐานลายตาราง ซึ่งเป็น $In_{0.2}Ga_{0.8}As$ หนา 25 นาโนเมตร บนแผ่นฐานแกลเลียมอาร์เซไนด์ คุณสมบัติทางสัณฐานวิทยาและทางแสงของโครงสร้างที่มีขนาดเล็กในระดับนาโน ถูกศึกษาด้วยกล้องจุลทรรศน์แรงอะตอม (atomic force microscope, AFM) และการทดลองโฟโตลูมิเนสเซนส์ (photoluminescence, PL)

ลักษณะทางสัณฐานวิทยาของโครงสร้างในระดับนาโนบนพื้นผิวลายตารางแตกต่างกันอย่างมีนัยสำคัญ ซึ่งขึ้นอยู่กับบริเวณ และสามารถสรุปได้ดังนี้ บนบริเวณพื้นผิวเรียบโครงสร้างในระดับนาโนพัฒนาจากโครงสร้างนาโนโฮล (nanoholes, NHs) ไปเป็นนาโนพล็อพเพลเลอร์ (nanopropellers, NPs) และ QDMs ซึ่งมีความสม่ำเสมอและเหมือนกันกับโครงสร้างที่ปลูกบนแผ่นฐานแกลเลียมอาร์เซไนด์เรียบ บนบริเวณเส้นมิสฟิทดิสโลเคชัน (misfit dislocation, MD) ในทิศ [110] ความเครียดบนพื้นผิวส่งผลต่อความสมมาตรของโครงสร้างในระดับนาโน และในบางกรณีมีการพัฒนาไปเป็นโครงสร้างรูปแบบใหม่เช่น NHs ที่มีรูปร่างเป็นข้าวหลามตัด ควอนตัมดอต (quantum dots, QDs) ที่มีฐานเป็นรูปข้าวหลามตัด และ NPs ที่มีลักษณะเหมือนหน่วยพื้นฐานของควอนตัมเซลลูล่าออตโตมาต้า (quantum cellular automata) บนบริเวณเส้น MD ในทิศ [1-10] การกลบด้วยชั้นบางของแกลเลียมอาร์เซไนด์ก่อให้เกิด NHs และเส้นของเนินในระดับนาโน (nanomounds) ส่วนการปลูกซ้ำด้วยอินเดียมอาร์เซไนด์ก่อให้เกิด QDs ที่มีฐานเป็นรูปข้าวหลามตัดบน NHs และQDs บนสันและขอบของแนวเส้นในระดับนาโน

การวัด PL ของโครงสร้าง QDMs บนแผ่นฐานลายตารางแสดงให้เห็นว่า โครงสร้างโดยรวมปล่อยสัญญาณอย่างเด่นชัดในช่วงกว้างตั้งแต่ 0.89 -1.6 eV ซึ่งบ่งชี้ถึงคุณภาพโครงผลึกที่สูง อิทธิพลของการอพพยของพาหะจาก QDs ขนาดเล็ก ไปสู่ QDs ขนาดใหญ่ถูกสังเกตุเมื่ออุณหภูมิสูงขึ้น

ลักษณะทางสัณฐานวิทยาอันหลากหลายที่ถูกพบในงานนี้อาจขยายขอบเขตของวัสดุและสิ่งประดิษฐ์ทางออปโตอิเล็กทรอนิกส์ที่เป็นประโยชน์ในช่วงอินฟราเรดใกล้ (near infrared)

จุฬาลงกรณ์มหาวิทยาลัย
CHULALONGKORN UNIVERSITY

ภาควิชา	วิศวกรรมไฟฟ้า	ลายมือชื่อนิสิต
สาขาวิชา	วิศวกรรมไฟฟ้า	ลายมือชื่อ อ.ที่ปรึกษาหลัก
ปีการศึกษา	2558	

5670259721 : MAJOR ELECTRICAL ENGINEERING
KEYWORDS: INAS / INGAAS / CROSS-HATCH PATTERNS / SELF-ASSEMBLED QUANTUM DOT MOLECULES / MOLECULAR BEAM EPITAXY

NITAS NAKARESEISOON: InAs quantum dot molecules on nanohole/cross-hatch pattern templates. ADVISOR: ASSOC. PROF. DR. SONGPHOL KANJANACHUCHAI, 54 pp.

This thesis studies the evolution and characteristics of quantum dot molecules (QDMs) on cross hatch patterns (CHPs). QDMs are grown by a partial-capping-and-regrowth technique on CHP templates which are 25-nm $In_{0.2}Ga_{0.8}As$ on GaAs substrates. The morphological and optical properties of the nanostructures are studied by atomic force microscope (AFM) and photoluminescence (PL), respectively.

The morphologies of nanostructures on CHPs vary significantly depending on the areas and can be concluded as follows. On Flat areas, the nanostructures develop from nanoholes (NHs) to nanopropellars (NPs) and QDMs which are uniform and similar to those grown on flat GaAs substrates. On [110] misfit dislocation (MD) lines, the strain affects the symmetries of nanostructures, and some of them transform to new types of nanostructures: diamond-shaped NHs, diamond-based QDs, and NPs which resemble a quantum cellular automata (QCA) unit cell. On [1-10] MD lines, partial capping of GaAs creates NHs and stripes of nanomounds; the regrowth of InAs creates diamond-based QDs on the NHs, QDs on the edge of the stripes, and QDs on the ridge of the stripes

PL measurements of QDMs on CHPs show that the entire structure strongly emits broad signals in the 0.89-1.6 eV range, indicating high crystalline quality. At high temperature, the effects of carrier migration from small QDs to large QDs are observed.

The rich morphologies observed in this works may increase the range of useful optoelectronic materials and devices in the near infrared.

Department:	Electrical Engineering	Student's Signature	....
Field of Study:	Electrical Engineering	Advisor's Signature	....
Academic Year:	2015		

ACKNOWLEDGEMENTS

Firstly, the author would like to express sincere gratitude to his adviser, Assoc. Prof. Dr. Songphol Kanjanachuchai, for the patience, motivation, enthusiasm, and invaluable comments. He has been a powerful role model for the author since the Bachelor's degree. Without his guidance and support, the study would not have been completed. Also, the author appreciates Prof. Somsak Panyakeow, the chairperson and director of Semiconductor Device Research Laboratory (SDRL), for the seminar session which always gives the inspiration, knowledge, and opportunities to practice presentation. The special thanks go to Dr. Noppadon Nuntawong, the external examiner from National Science and Technology Development Agency (NSTDA), for interesting questions and warm comments during the examination.

The author gratefully acknowledges all staff members of SDRL: Mr. Supachok Thai noi, the first-choice supporter for any laboratory problems; Mrs. Kwanruan Thainoi, the generous lab secretary; Mr. Pattana Phuntunwong, the powerful mechanical technician; and Mr. Porn chai Changmoang, the skillful electrical technician.

จุฬาลงกรณ์มหาวิทยาลัย
CHULALONGKORN UNIVERSITY

The author also thanks for the collaborations and colorful memories from seniors, juniors, and lab fellows, in particular Mr. Win Eiwwongcharoen and Mr. Beni Adi Trisna who have been walking together through the difficult times of MBE-system maintenance.

Last but not lease, the author would like to express his deepest gratitude to the family: his mother, Mrs. Muthita Nakareseisoon; and his brother, Mr. Vitid Nakareseisoon, for financial and emotional supports.

CONTENTS

Page

THAI ABSTRACT iv

ENGLISH ABSTRACT v

ACKNOWLEDGEMENTS vi

CONTENTS vii

LIST OF FIGURES ix

LIST OF TABLES xiii

CHAPTER 1 Introduction 1

1.1 Historical background and motivation 1

1.2 Objective 3

CHAPTER 2 Literature review 4

2.1 From bulk to low-dimensional semiconductors 4

2.2 Semiconductor QDs 6

2.2.1 Properties and applications of QDs 6

2.2.2 Semiconductor quantum dot synthesis 7

2.2.3 Epitaxy technique 8

2.2.4 Self-assembled quantum dot 10

2.3 The studies of self-assembled InAs QDs 12

2.4 The studies of self-assembled NHs 16

2.5 The studies of self-assembled QDMs 21

CHAPTER 3 Research methodology 23

3.1 Molecular beam epitaxy 23

3.1.1 RIBER 32P MBE machine 23

3.1.2 RHEED 25

3.1.2.1 Temperature calibration for sample surface 27

3.1.2.2 Growth-rate calibration for Ga 28

3.1.2.2 Growth-rate calibration for indium 30

3.1.3 Experimental procedures 30

3.1.3.1 Conventional sample preparation 30

Page

3.1.3.2 QDMs on CHPs growth procedure 31
3.2 Atomic Force Microscopy 33
3.3 Photoluminescence 34
CHAPTER 4 Experimental results and discussion 36
4.1 Review on the characteristics and nucleation of QDs on CHPs 36
4.2 The evolution of QDMs on CHPs 40
4.2.1 Flat surfaces 41
4.2.2 [110] MD lines 44
4.2.3 [1-10] MD lines 53
4.3 Optical properties of QDMs on CHPs 57
4.3.1 Power-dependent PL 57
4.3.2 Temperature-dependent PL 60
CHAPTER 5 Conclusions 62
REFERENCES 64
VITA 69

จุฬาลงกรณ์มหาวิทยาลัย
Chulalongkorn University

LIST OF FIGURES

Figure 2.1 Schematic illustrating the formation of energy bands in crystalline silicon [17]. 4

Figure 2.2 Schematic views and density of states (DOS) for bulk, quantum well, quantum wire and quantum dot [18]. 5

Figure 2.3 Schematic illustrating two QD synthetic methods: (a) bottom-upand (b) top-down [20]. 8

Figure 2.4 Schematic representation of (a) homoepitaxy, (b) heteroepitaxy with compressive strain, and (c) heteroepitaxy with tensile strain [21]. 9

Figure 2.5 (a) Equilibrium phase diagram as a function of growth thickness H and lattice misfit Ɛ; the small panels illustrating the surface morphologies in six growth modes. The thickness (monolayer, ML) of wetting layer n_1, island coverage n_2, size x_0 and density ρ as a function of H in the case of (b) $Ɛ_1 < Ɛ < Ɛ_2$ and (c) $Ɛ_2 < Ɛ < Ɛ_3$[22]. 11

Figure 2.6 Schematic illustrating QDs formation due to elastic strain relaxation [21]. 12

Figure 2.7 AFM images of GaAs substrates overgrown with (a) 0.5-ML, (b) 1.0-ML, (c) 1.5-ML, (d) 1.8-ML, and (e) 2.2-ML InAs [21]. Close-up (f) TEM image and (g) schematic diagram of InAs QDs[23]. 12

Figure 2.8 (a) Schematic representation of local strain energy densities before and during QD formation [24]. (b) Schematic illustrating In atoms detachment from 2D islands to QDs in the early state of QD nucleation [21]. 14

Figure 2.9 AFM images of 1.8-ML InAs QDs fabricated with (a) 0-s, (b) 30-s, (c) 60-s, and (d) 120-s GIs [21]. 15

Figure 2.10 AFM images of 1.8-ML InAs QDs fabricated at (a) 515°C, (b) 493°C, (c) 470°C, and (d) 450°C [25]. 15

Figure 2.11 AFM images of 1.8-ML InAs QDs fabricated with the InAs growth rates of (a) 0.005 ML/s, (b) 0.008 ML/s, (c) 0.03 ML/s, (d) 0.04 ML/s, (e) 0.06 ML/s, (f) 0.1 ML/s, (g) 0.2 ML/s, and (h) 0.4 ML/s [25] 16

Figure 2.12 AFM images of (a) nanoholes, (b) nanopropellars,(c) quantum dot molecules [27] and (d) quantum dot chains [28]. 16

Figure 2.13 AFM images and corresponding oblique 3D views of 1.8-ML InAs QDs overgrown with (a) 0-ML, (b) 3-ML, (c) 6-ML, (d) 15-ML, (e) 30-ML GaAs [30]. Linescans of the nanostructures along (f) [1-10] and (g) [110] directions [31]. 17

Figure 2.14 Schematic illustrating the effects of thin GaAs capping on (a) Ga local surface strain energy μ and (b)-(c) In elastic energy and wetting chemical potential $\Omega E_s(r)$- $\zeta\Omega\vartheta(r)a$ [25]. 17

Figure 2.15 Schematic illustrating the evolution from QDs to NHs during GaAs capping process [32]. 17

Figure 2.16 AFM images, linescans along [1-10] direction, and corresponding histograms for the depths and widths of the NHs grown with (a) 30-s, (b) 40-s, (c) 80-s GIs [33]. 19

Figure 2.17 AFM images of InAs QDs overgrown with 10-ML GaAs at (a) 500°C, (b) 480°C, (c) 440°C, and (d) 400°C [34]. 19

Figure 2.18 AFM images of the nanostructure evolution during GaAs capping at (a)-(c) low (0.08 ML/s) and fast (0.6 ML/s) rates [32] 20

Figure 2.19 AFM images of NHs overgrown with (a) 0.6-ML, (b) 0.9-ML, and (c) 1.2-ML InAs [29] 21

Figure 2.20 Schematic illustrating the evolution from QDs to QDMs through the partial-capping-and-regrowth technique [35]. 21

Figure 2.21 AFM images of (a) NPs and corresponding QDMs grown at (a) 470°C, (b) 450°C, and (c) 430°C. [36] 22

Figure 3.1 (a) RIBER 32P (left) and RIBER Compact 21 (right) solid-source MBE machine at faculty of electrical engineering, Chulalongkorn University. (b) Schematic diagram of RIBER 32P MBE machine [26]. 23

Figure 3.2 (a) Growth chamber of RIBER 32P MBE machine taken from side view. (b) Schematic diagram of growth chamber displayed from top view [37] 24

Figure 3.3 (a) Schematic diagram of RHEED technique [25] and examples of diffraction patterns on a fluorescent screen: (b) streaky patter indicating flat surface, (c) de-oxidation pattern, and (d) spotty pattern indicating InAs QDs. 26

CHULALONGKORN UNIVERSITY

Figure 3.4 Temperature profile of temperature calibration for sample surface and RHEED diffraction patterns relative to four critical points (T1 – T4). 27

Figure 3.5 (a) Surface reconstruction of 1-ML GaAs and (b) corresponding RHEED intensity from state A to E [39]. (c) RHEED-intensity oscillation during GaAs deposition [40]. 29

Figure 3.6 Schematic cross-sectional diagrams of samples (a) A—nanoholes, (b) B—nanopropellers, and (c) C—QDMs on CHPs. 32

Figure 3.7 A temperature profile of growth procedures for samples A, B, and C. ...32

Figure 3.8 AFM characterization (a) picture of Seiko SPA-400 at SDRL and (b) schematic diagram describing the operating principle [41]. 33

Figure 3.9 (a) A schematic diagram of a PL phenomenon in semiconductor [42]. (b) Components and setup for a PL experiment. 34

Figure 4.1 (a) Schematic cross-sectional diagram of QDs on CHPs sample studied by Thitipong Chokamnui (2013). (b) A 10 × 10 μm^2 AFM image of the sample with an 2 × 2 μm^2 inset magnified around the cross sections [43]. 37

Figure 4.2 Two-dimensional simulated strain distributions of (a) [110] and (b) [1-10] MD. (c) A combined strain distribution at the cross section. (d) A 200 × 200 nm^2 AFM image of a QD on the cross section with dash lines guiding the orthogonal dislocation lines [46]. 38

Figure 4.3 (a) A 2 × 2 μm^2 AFM image of QDs on CHPs nanostructure. (b) A corresponding simulated strain distribution. (c) An overlapped image of the strain distribution and AFM image [45]. 39

Figure 4.4 10 × 10 μm^2 AFM images with 2 × 2 μm^2 inset magnified around the cross sections of (a) sample A, (b) sample B, and (c) sample C. 40

Figure 4.5 600 × 600 nm^2 AFM images inserted with small oblique 3D views of (a) sample A, (b) sample B, and (c) sample C. Linescans along the [1-10] direction of a typical (d) NH from sample A and (e) NP from sample B. (f) A linescan of QDM along given line in figure 4.5(c). 41

Figure 4.6 (a) A 2 × 2 μm^2 AFM image of stand-alone normal QDs and QDMs on flat areas of sample C. (b) A corresponding height histogram of QDs. 43

Figure 4.7 2 × 2 μm^2 AFM images (upper panels) and oblique 3D views (lower panels) along [110] MD lines of sample (a) A, (b) B, and (c) C. 44

Figure 4.8 (a) A 0.8 × 1.6 μm^2 AFM image at [110] MD lines of sample A. (b and c) Close-up AFM images and oblique 3D views from two different locations. (d) Linscans of a NH on flat surface (NH0) and a [110] MD line (NH1 - NH5) from figure 4.8(b)-(c). 45

Figure 4.9 (a) A 5 × 5 μm^2 AFM image at a [110] MD line of sample B. 800 × 800 nm^2 AFM image retrieved from (b) box1 and (c) box2 area in figure 4.9 (a). 48

Figure 4.10 (a-c) 800 × 800 nm^2 AFM images and oblique 3D views at [110] MD lines of sample B. (d) Linescans in the [110] direction of QDs in figure 4.10 (a) and figure 4.10 (b). (e) Linescans in the [1-10] direction of NP1 – NP5 in figure 4.10 (c). 48

Figure 4.11 (a) 120 × 80 nm^2 AFM images and (b) oblique 3D views of a NP which is occupied by 4 QDs. (c) The schematic diagram of two QCA unit cells [49]. 49

Figure 4.12 (a) A 2 × 5 μm^2 AFM image at a [110] MD line of sample C. (b and c) Close-up AFM images and oblique 3D views from two different locations... 51

Figure 4.13 The height histogram of QDMs and nQDs (solid line) on a [110] MD line from figure 4.11(b) and QDMs (dash line) from a neraby flat area. 51

Figure 4.14 2 × 2 μm^2 AFM images and oblique 3D views at [110] MD lines of (a) sample A , (b) sample B, and (c) sample C. (d - g) Linescans in the [110] direction of the given lines of the three AFM images. 53

Figure 4.15 (a) A Height histrogram of rQDs and eQDs (solid line) on a [1-10] MD line from figure 4.13 (c) and QDMs (dash line) of a neraby flat area. (b) A 2 × 2 um^2 AFM image and corresponding height histrogram of dQDs. 55

Figure 4.16 AFM images at (a) [110] and (b) [1-10] MD lines of sample C. 56

Figure 4.17 20-K PL spectra results of QDMs on CHPs measured in power-dependent experiment and accompany with a small inset of power-dependent peak intensity. 58

Figure 4.18 (a) Spectra simulated by Gaussian-fitting method. (b) A comparison between simulated and experimental spectra measured at 20 K and 90-mW laser power. 59

Figure 4.19 PL spectra resuls of QDMs on CHPs measured in temperature-dependent experiment at 90-mW laser power. 61

LIST OF TABLES

Table 4.1 The average dimensions of QDs on flat areas and two orthogonal MD lines obtained from AFM image in figure 4.1(b) [44]....................37

Table 4.2 The average dimensions of representative NHs (NH0 – NH5) from AFM images in Figs 4.8 (b) and (c)..45

Table 4.3 The summary of QDs that are observed in sample C 56

CHAPTER 1
Introduction

1.1 Historical background and motivation

Nowadays, electrical devices have become more essential to human life. Every activity from day to night is concerned with the electrical devices. They make daily life become more convenient. Children can acquire knowledge easier via smart phones. Human has longer lifespan thank to the medical equipment. While social livelihood is improving due to these technologies, the shortage of energy has become a huge obstacle. The amount of oil, a primary energy resource, is decreasing rapidly because of an every-year-rising demand of energy. The world has reached the oil peak point since 2014 [1]. After this critical point, the oil production will become more difficult which affects to the crude-oil price. Nuclear energy was supposed to be the solution of this problem; however, after Fukushima Daiichi Nuclear Power Plant disaster (2011), the world had realized the hazard of nuclear radiation, and Japan government, decided to shut down around 50 reactors one year later. Now people are seeking for a green, sustainable, and efficient source of energy; it is saying that 21 Century is the period of transition from dirty fuel to clean energy resource.

จุฬาลงกรณ์มหาวิทยาลัย
CHULALONGKORN UNIVERSITY

A combination of alternative energies—such as hydroelectric, geothermal, biomass, solar, and wind energy—should be the solution for the energy crisis. The solar energy is one of the most prevalent renewable energy resources due to several outstanding features: for example, silent operation, low maintenance, and availability in every place. Solar radiation can be converted to electricity directly via solar cells, and this phenomenon is called Photovoltaic effect. When photons, light particles, incident to a solar cell, they are absorbed, and electron-hole pairs are generated. Then, by the internal electric field, the electrons and holes are separated immediately to a negative and a positive terminal, thus generating electricity. The first solar cell, invented by Charles Fritts in 1883, made use of Schockley barrier between selenium and gold; however, the efficiency was still low (~1%). Today, a conventional solar cell is made from a silicon-based p-n junction with the efficiency around 12-15%. The

best single-junction solar cell, holding the world's record in efficiency at 28.8%, is made from gallium arsenide (GaAs) [2]. Theoretically, Shockley and Queisser predicted that the maximum efficiency of a single-junction solar cell is 33% and the bandgap value should be 1.3-1.4 eV, which fits to that of GaAs [2]. The limitation comes from the fact that solar radiation is broadband—including infrared, visible light, and ultraviolet—whereas a single-junction and single-material solar cell can efficiently absorb only on one range of the solar radiation.

To exceed the limitation, many strategies have been proposed: namely, tandem, quantum dot, impact ionization and hot-carrier solar cells [3-5]. However, only the first two methods are plausible. A tandem solar cell uses multi junction and materials to absorb broader range of the solar radiation. Currently, the world-record solar cell is the four-junction tandem solar cell with the efficiency of 44.7%[6]. A quantum dot solar cell, on the other hand, is based on single junction; it exploits the properties of quantum dots (QDs), small semiconductor particles (~2-20 nm), to increase the efficiency. When embedded in the solar-cell junction, QDs introduce intermediate bands to the energy structure, and extra photons, therefore, can be absorbed through these bands. The energy levels of intermediate bands are adjustable by either the material compositions or QD sizes. With the optimal energy levels, the efficiency of intermediate band solar cell is predicted to be as high as 74.6% [7]**.** In practice however, QD solar cells have low performance (>12% efficiency) [8]. Although generated current increases, it turns out that the voltage drops due to the strain effects and energy coupling between the intermediate and the host-material bands [9]. The large gap between the efficiency in theory and experiment may imply that we do need to research more about this kind of solar cell. Especially, QDs have many unique phenomena, such as two-step photon absorption, multi-exciton generation, thermal excitation and tunneling effect. Moreover, in order to create a high current, the QD density should be high; both material composition and QD sizes need to be well controlled so that the solar cells can absorb broad spectrum.

The model for multi-stacked different-sized QDs was proposed with an attempt to fabricate "rainbow solar cell", illustrating the solar cell with the potential to effectively absorb the large parts of solar spectrum [10]. However, it has been proven

that stacking many QD layers introduces strain, resulting in lower voltage and efficiency. Conversely, there is another interest to fabricate multi-sized QDs on a single layer. At Semiconductor Device Research Laboratory (SDRL), Chulalongkorn University, many types of nanostructures have been investigated, such as QDs on cross-hatched templates, QD molecules (QDMs), quantum rings and quantum wires [11-14]; the first two structures have the high potential for broad-band applications. The QDMs, fabricated by a partial-capping-and-regrowth technique, each consist of one big QD in the middle and several small QDs around. By appropriate stacking double layers of QDMs, the photoluminescence (PL) results a wide spectrum with the FWHM of 170 meV, which are the integration from four QD peaks [15]. The QDs on cross-hatched templates are fabricated by two procedures: cross-hatched-pattern fabrication and QD nucleation. Guided by cross-hatched strains, some QDs line along the [110] and [1-10] directions. In addition, QD-size diversity is observed at four different locations: flat area, [110] misfit dislocation, [1-10] misfit dislocation and the intersection; therefore, the PL spectrum of this structure is broad as the combination of the four QD peaks [16].

1.2 Objective

The objectives of this research are to study the evolution QDMs on cross-hatched template grown by MBE technique and to characterize the nanostructures in both morphological and optical aspects.

CHAPTER 2
Literature review

This chapter provides background knowledge from bulk semiconductors to nanostructures which are quantum dots (QDs) and quantum dot molecules (QDMs). For the QD and QDM sections, this thesis interest InAs QDs and QDMs grown by a partial-capping-and-regrowth technique. Most of the experiments have been conducted by researchers in *Semiconductor Device and Research Laboratory (SDRL).* The details include the nucleation mechanisms, the characteristics, the effects of growth parameters, and the potential applications.

2.1 From bulk to low-dimensional semiconductors

Solid-state physics, the study of how solid-matter properties result from atomic properties, has been significantly influenced by the development of quantum mechanics. Fig. 2.1 shows the electronic structures of Si from separated atoms to bonding atoms and crystal. As two atoms are interacting, their atomic orbitals just combine and form molecular orbitals. However, for the crystals that many atoms are densely packing together, their discrete molecular orbitals split, according to Pauli exclusive principle, into band orbitals whose energies fall in continuous range called energy bands, and how electrons occupy in these bands is explained Fermi-Dirac—

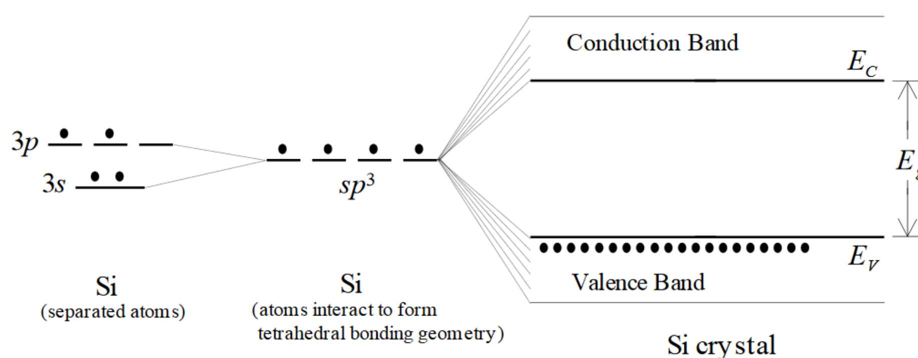

Figure 2.1 Schematic illustrating the formation of energy bands in crystalline silicon [17].

distribution. At 0 K, the top fully-filled, by electrons, band is called valence band, while separated by energy gap (E_g), the bottom empty band is called conduction band. When the temperature increases (>0 K), electrons are thermally excited and transfer from valence band to conduction band, leaving empty spaces called holes. The generated electrons and holes are charge carriers; therefore, electrical conductivity of each material depends on the density of these particles. The energy gap (or band gap) value is the significant parameter to determine materials as three electrical types: metal, semiconductor, and insulator.

However, when it is reduced to the low dimension relative to de Brogile electron wavelength of (~20 nm at 300 K), the situation changes. Electrons are allowed to oscillate at certain wavelengths to fulfill the wave standing conditions. In conclusion, the electron energy states in the confined direction, surprisingly, turn back to discrete levels. Fig.2.2 shows the schematic views and the density of states for bulk and low-dimensional semiconductors, which the structures are called quantum wells for confinement in 1D; quantum wires, 2D; and quantum dots, 3D.

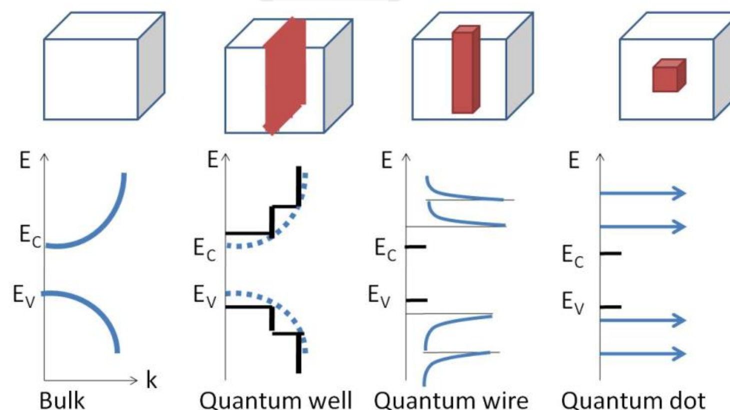

Figure 2.2 Schematic views and densities of states (DOS) for a bulk, quantum well, quantum wire and quantum dot [18].

2.2 Semiconductor QDs

2.2.1 Properties and applications of QDs

Quantum dots (QDs) are versatile nanostructures. The devices made from QDs are low cost, low energy consumption, but high efficiency due to their small dimensions and confinement properties. QDs are utilized in many fields of applications because of their unique properties:

- **Quantum computer.** QDs confine electrons in every direction, and the density of states is delta functions; these are key properties to make quantum computer. Instead of a normal "bit" that is used for the two memory-state units ("0" or "1") in classical computers, a *quantum bit* (or qubits) has infinite number of possible states as a combination between basis states ("0" and "1") and the probabilities, due to the uncertainty principle. For example, a qubit state can be "0" with 25% and "1" with 75%, or "0" with 50% and "1" with 50%, or 80% and "1" with 20%, and so on. To demonstrate how powerful the qubit is, it was calculated that only 30 qubits are equivalent to about 10^9 transistors, typical of a personal computer. Many strategies have been proposed to make qubits: including, photon polarization, electron charge, and electron spin. The last strategy is feasible by two coupled gated QDs: the system of double QDs that an electron in each QD has the opposite spin to the other, and the electron energy levels can be manipulated by metal-top-gate voltage [19].

- **Quantum dot laser**. Another interesting QD property is to trap electrons and holes for radiative recombination. Differ from other light source, laser is high coherence: monochrome (single wavelength), single phase, directionality, and high intensity. Generally, the laser device's components are gain media, energy-pumping source, and cavity; in the case of QD lasers, they are QDs, electricity (electrons and holes), and dielectric-mirror cavity, respectively. The QD lasers operate by injecting electrons and holes into the active region, where they are trapped in QDs. Then, photons are emitted due to the carrier recombination, and the intensity is amplified by the stimulated recombination of the electrons and holes in QDs; until the density is high enough, laser can pass through one side of dielectric mirrors. Because of the carrier trapping property, the threshold current is significantly low even at room temperature, compared to those of bulk and quantum well laser.

Chulalongkorn University

- **Quantum dot solar cell**. As discussed in Chapter1, the size-dependent tunable band gap is used to adjust QD intermediate bands so that the solar cells absorb broad range of solar spectrum, thus increasing current and efficiency.

- **Thermoelectric device**. In the case of low dimensions, electrons behave like a wave with probability density. This means that they can tunnel through QDs if the distance is small enough; this fact is applied to thermoelectric devices. Thermoelectric devices convert thermal to electrical energy, or vice versa. The good materials for thermoelectric devices need to have high electrical conductivity, but low thermal conductivity. It turns out the QDs with appropriate dimensions can filter phonon, while electron can tunnel through QDs.

2.2.2 Semiconductor quantum dot synthesis

The practical QDs exploit the hetero-junction of two different semiconductors as a finite potential well. Therefore, carriers are confined inside QDs. There are two methods to synthesize QDs: top-down and bottom-up.

1. **Top-down method**. Starting from bulk semiconductors, the materials are removed by certain technique in order to approach the designed dimensions. A common technique is using an electron beam lithography followed by lift-off processes, or etching. Also, it can fabricate by directly sputtering focused ion beam to the surface of semiconductors. The strength of top-down method is that complex nanostructures are feasible within the limit size of 20 nm, whereas the drawbacks are defects and impurities due to the chemical process, which may later degrade the efficiency of devices.

2. **Bottom-up method**. Conversely, this method utilizes self-assembling of each atom to form nanostructures. Many techniques have been proposed: for instance, microemulsion, hot-solution decomposition, microwaves, sol-gel, and molecular beam epitaxy (MBE). We will focus on the MBE technique which is used in this study. MEB is widely used for compound semiconductor due to the advantages of high purity and crystal perfection. However, disadvantages of this method are the randomness in both size and position of nanostructures.

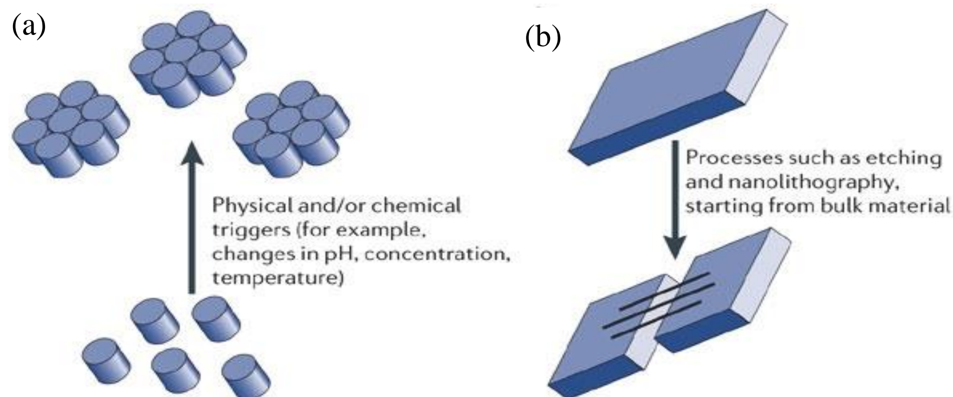

Figure 2.3 Schematic illustrating two QD synthetic methods: (a) bottom-upand (b) top-down [20].

2.2.3 Epitaxy technique

Epitaxy is an essential technique for crystal growth for both industrial and research fields as it allows users to deposit a crystalline overlayer on a crystalline substrate. Coming from Greek root, the term *epitaxy* is composed of “epi”, meaning above, and “taxy”, meaning an order manner. The word gives the sense of material growth on the surface with high order alignment. In the case semiconductor devices, epitaxy is used to create an active region—an area where the crucial phenomena occur such as a p-n junction in solar cell—onto a substrates, which is an epi-ready, high-quality, and mass-produced semiconductor wafer that used as support platforms. In the case of laboratories, epitaxy is used to fabricate and study many kinds of structures, or it is used to demonstrate certain concept due to the flexibilities: several parameters are adjustable with high accuracy such as material compositions, temperatures, deposition rates and thickness. The common methods for epitaxy techniques are vapous-phase epitaxy (VPE), liquid phase epitaxy (LPE), and molecular beam epitaxy (MBE).

Judging from the materials, if the deposited layer and substrate are the same materials, it called homoepitaxy; if not, heteroepitaxy. Homoepitaxy as shown in Fig. 2.4 (a) is generally used for the surface treatment: because the semiconductor substrate’s surfaces are originally covered by native oxide; therefore, before growing a real structure, the substrates must undergo preheat process and followed by homoepitaxy to flatten the surfaces. Also, silicon solar cells are fabricated by

homoepitaxy. In the case of heteroepitaxy, strains are introduced to the structure if lattice sizes of substrate and deposited material are different, called lattice mismatch. Fig. 2.4 shows two types of heteroepitaxy strains: (a) compressive for the deposition of smaller lattice than the substrate, and (b) tensile for the deposition of larger lattice than the substrate. The degree of accumulated strain depends on two parameters: film thickness and lattice misfit, $\varepsilon = \frac{(d_A - d_B)}{d_B}$. Strains can deform both crystal and electronic structures: the periodicity and lattice potential are associated with a band gap, and the new band gap under strain condition can be calculated by Perturbation theory. However, if the accumulated strains are so high that they can break the crystal bonding, the crystal will be permanently deformed and the process is called strain relaxation. The strain relaxation usually transforms the crystal structures into unfavorable defects, but sometimes it is exploited to fabricate certain nanostructure, such as QDs.

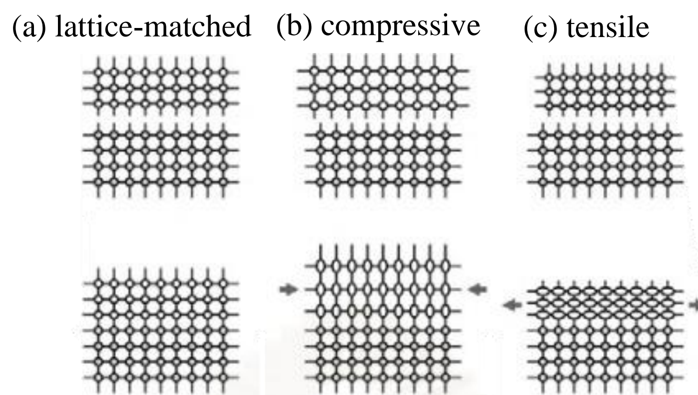

Figure 2.4 Schematic representation of (a) homoepitaxy, (b) heteroepitaxy with compressive strain, and (c) heteroepitaxy with tensile strain [21].

2.2.4 Self-assembled quantum dot

Self-assembled QDs are the results of strain relaxation in lattice-mismatch heteroepitaxy. The formation of self-assemble QDs has been intensively studied since the last decade. At the beginning, a QD was thought as a defect that degrades semiconductors. Until 1993, Leonard et al. discovered that InGaAs QDs, surprisingly, were dislocation free structures that confine electron in every direction. The discovery has unveiled new paths of semiconductor devices, and drawn a large number of group investigating the physical properties with an aim to fabricate new kind of device. In fact, self-assembled QDs are found in many semiconductor systems, such as Ge/Si, InAs/GaAs, and InAs/InP. The explanations of QDs formation, size and density, are complicated as they are associated with equilibrium and non-equilibrium effects. For the former case, the phase diagram of growth modes, as a function of epitaxy thickness H and lattice mismatch ε, was proposed by Daruka et al (1997) [22]. They classified the surface morphologies into four modes:

(1) Frank van der Merve (FM) mode for *wetting layers (WLs)*, 2D structures,
(2) Volmer Weber (VW) mode for *defect-free QDs*, 3D structures,
(3) Stranski Krastanow (SK) mode for defect-free QDs on WLs,
(4) Ripened (R) mode for large and high-strain QDs causing dislocations as capping.

It should be noted that the model omits material desorption and non-equilibrium effects, such as the growth rate and temperature, which we will cover later. Figs. 2.5 shows the development of heteroepitaxy—i.e., the material amount n (ML) of WLs and QDs—for (b) low lattice mismatched ($\varepsilon_1 < \varepsilon < \varepsilon_2$) and (c) high lattice mismatched ($\varepsilon_2 < \varepsilon < \varepsilon_3$) systems, respectively; moreover, the high x (nm) and density ρ (unit/cm^3) of QDs are shown as well.

จุฬาลงกรณ์มหาวิทยาลัย
CHULALONGKORN UNIVERSITY

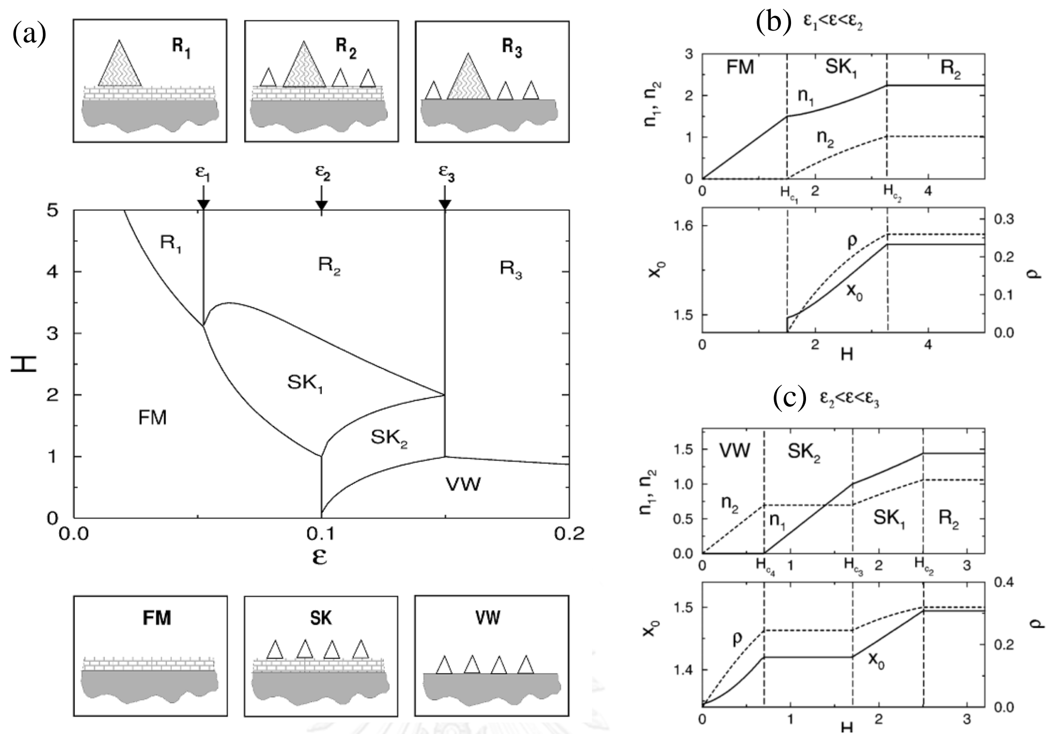

Figure 2.5 (a) Equilibrium phase diagram as a function of growth thickness H and lattice misfit ε; the small panels illustrating the surface morphologies in six growth modes. The thickness (monolayer, ML) of wetting layer n_1, island coverage n_2, size x_0 and density ρ as a function of H in the case of (b) $\varepsilon_1 < \varepsilon < \varepsilon_2$ and (c) $\varepsilon_2 < \varepsilon < \varepsilon_3$ [22].

- **Low lattice mismatch ($\varepsilon_1 < \varepsilon < \varepsilon_2$)** such as InAs/GaAs ($\varepsilon$=7%), Ge/Si ($\varepsilon$ =4.2%). The growth mode starts with FM mode, in which the deposited material increases the thickness of WL, as well as accumulated strains. Until the deposition reaches the critical thickness, strain relaxation spontaneously forms QDs as illustrated in Fig. 2.6, and system enter SK mode. In this mode, the QD height and density increase; Also, the WL thickness increases but with lower rate than the case of the FM mode. The critical thickness is corresponded to lattice-mismatch: the larger lattice mismatch results in the lower critical thickness. Finally, when the deposition thickness reaches another critical thickness, ripen QDs form, and the system enters R_2 mode, in which the deposited materials contribute to WL, finite QD, and ripen QDs.

CHULALONGKORN UNIVERSITY

- **High lattice mismatch ($\varepsilon_2 < \varepsilon < \varepsilon_3$)** such as InSb/GaAs ($\varepsilon$=14.3%). Because the high lattice mismatch creates high strains, QDs develop at the beginning of the deposition, and growth mode starts with VW mode. In this mode the deposited materials increase the QD height and density. Until the deposition reaches the critical thickness, QD development stops, and system enter SK2 mode, in which the deposited materials increase the WL thickness. For further deposition, system will reach SK1 and R2 modes the critical thicknesses which same as case of low lattice mismatch.

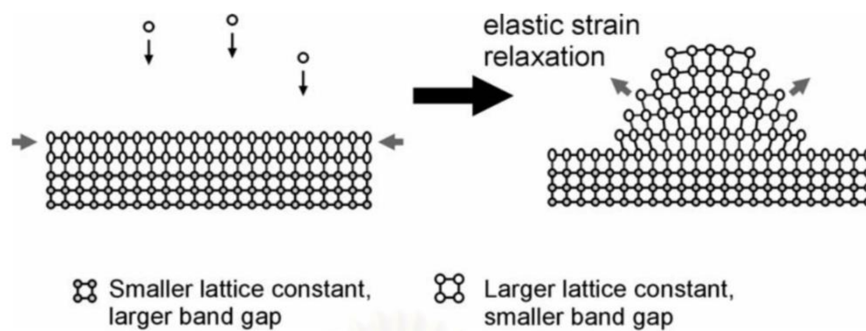

Figure 2.6 Schematic illustrating QDs formation due to elastic strain relaxation [21].

2.3 The studies of self-assembled InAs QDs

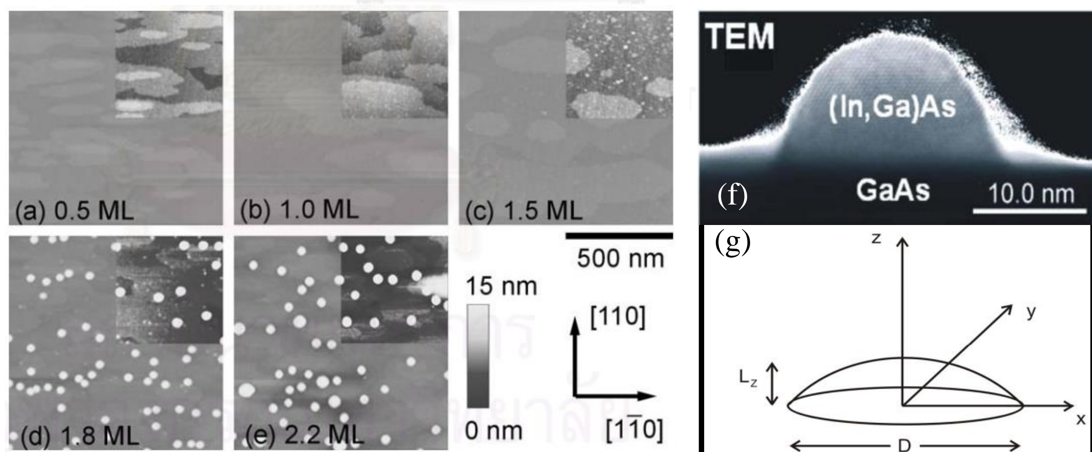

Figure 2.7 AFM images of GaAs substrates overgrown with (a) 0.5-ML, (b) 1.0-ML, (c) 1.5-ML, (d) 1.8-ML, and (e) 2.2-ML InAs [21]. Close-up (f) TEM image and (g) schematic diagram of InAs QDs[23].

This section aims to review InAs QDs grown on (001)-GaAs substrates by MBE technique. The contents include the sequence and mechanism of QDs formation, characterization of QDs, and the effects of growth parameters. Most of the experiments have been conducted by Kiravittaya and Songmung (SDRL laboratory, 2002) which the standard sample preparation will be presented in Section 3.1.3.1.

According to the equilibrium phase diagram (Fig. 2.5(a)), the lattice misfit between InAs and GaAs is 7.2%; therefore, the primary stage of InAs deposition on a GaAs substrate will give rise to a WL in SK mode, which dislocations do not formed yet. The surface morphology of GaAs substrates overgrown with sub-critical-thickness (<1.7ML) InAs at 500°C are shown in Figs. 2.7(a) – (c) [21]. For the InAs thickness lower than 1 ML (Figs. 2.7(a) and (b)), the surfaces look atomically flat, similar to GaAs deposition on the flat surfaces. The terrace steps with the thickness of 1 ML elongate along [1-10] direction due to an isotropic diffusion coefficient of In and Ga atoms in [1-10] and [110] directions. For the InAs thickness of 1.5 ML (Fig. 2.7 (c)), In atoms accumulate and form 2D islands, or so-called platelets, with the height of a few ML.

When the InAs deposition reaches the critical thickness of 1.7 ML, the system enters SK mode where 2D islands transform into 3D islands (or so-called QDs) as the results of strain relaxation. The surface morphology of GaAs substrates overgrown with 1.8-ML InAs is shown in Fig. 2.7(d). The average height and diameter of QDs are 10.7 nm and 37 nm; also, some 2D islands are observed on the surface. The close-up TEM image and schematic in Figs. 2.7(f) and (g) show the shape of an InAs/GaAs QD, which is described as a lenses shape: a circular base with long diameter (D) compared to the height (L_z). For the InAs thickness of 2.2 ML (Fig. 2.7 (e)), QDs become larger, and 2D islands disappear from the surfaces. However, the large InAs QDs have high tensile strains which can introduce dislocations during the capping process.

จุฬาลงกรณ์มหาวิทยาลัย
Chulalongkorn University

The nucleation mechanism and stability of InAs QDs can be described as follows. For the first few ML, the deposition will introduce strain to the flat surfaces due to the misfit between lattice constants of InAs and GaAs. There are driving forces which accumulate In atoms to form 2D islands, and therefore the local elastic strain energy increases with the volume of 2D islands. When the strain energy outweighs the surface energy, the transition from 2D to 3D islands occurs as a result of elastic strain relaxation, which reduces the system energy. Consequently, the local strain energy density is modified as Fig. 2.8 (a): the QD strain, especially in the middle of QDs, is lower than the flat surfaces, whereas the strain on the edge of QDs increases to the maximum points. The strain energy density is related to the surface chemical potential, which governs the dynamic behaviors of In atoms on the surfaces. This means In atoms prefer to dwell on the low-chemical-potential QDs, whereas the detachment of In atoms is prevent by the high-chemical-potential barriers around QDs. Moreover, as soon as QDs nucleate, In atom will detach from nearby 2D islands to QDs because the chemical potentials of QDs are lower than those of 2D island, as shown in Fig. 2.8(b). QDs act as In sinks; therefore, further In deposition will increase the size of QDs.

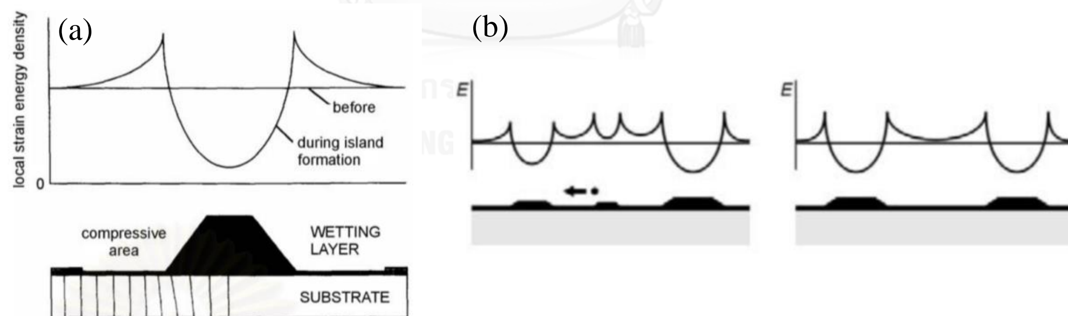

Figure 2.8 (a) Schematic representation of local strain energy densities before and during QD formation [24]. (b) Schematic illustrating In atoms detachment from 2D islands to QDs in the early state of QD nucleation [21].

The experiment was extended to investigated dynamic aspect of InAs QDs [19]. After the QD fabrication, the process was hold for a short duration (or so-called *growth interrupt (GI))* which was varied from 30s to 60s, and 120s. After that the temperature is step down immediately to freeze the sample surface, and the AFM images are shown in Fig 2.9. They found that after 30-s GI 2D islands disappear from the surface, and when GI was extended to 60 s and 120 s the size of QDs decrease due to As desorption at high temperature (500°C). Moreover, it turns out that the size homogeneity of QDs can be improve by inserting 30-s GI which gives rise to the narrowest PL linewidth compared to the other conditions.

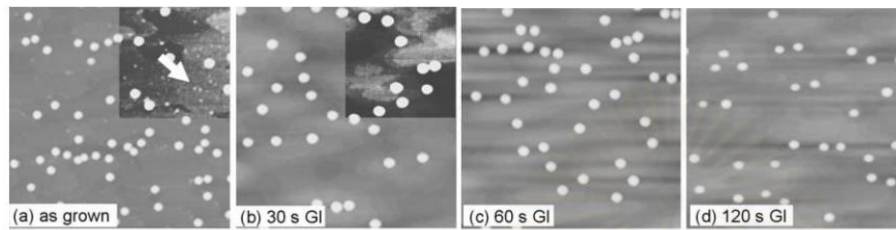

Figure 2.9 AFM images of 1.8-ML InAs QDs fabricated with (a) 0-s, (b) 30-s, (c) 60-s, and (d) 120-s GIs [21].

The effects of growth temperature were studied by growing InAs QDs at four different temperatures: 515°C, 493°C, 470°C, and 450°C [25]. The AFM results in Fig. 2.10 show that when the temperature decreases from 515°C to 450°C, the height of QDs decrease from about 14 nm to 5 nm, whereas the density increase from 1.0 x 10^9 cm^{-2} to 2.37 x 10^{10} cm^{-2}. The results are explained by the reduction of In diffusion length as the growth temperature decreases: If the diffusion of In atoms is low, they will form into small but high-density QDs. Moreover, QDs trend to form at the surface steps when the temperature is low (Fig. 2.10(d)).

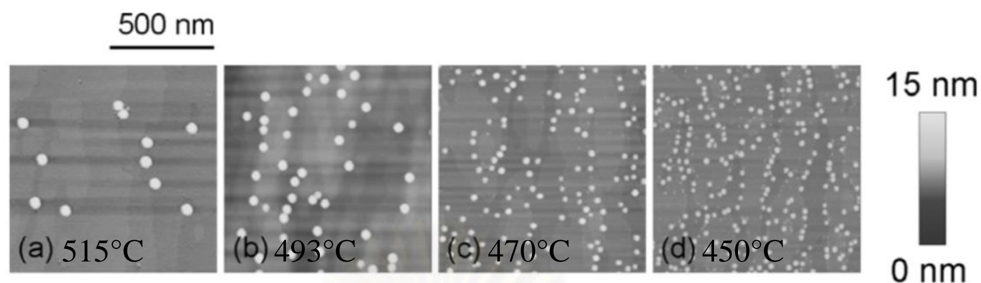

Figure 2.10 AFM images of 1.8-ML InAs QDs fabricated at (a) 515°C, (b) 493°C, (c) 470°C, and (d) 450°C [25].

The effects of InAs growth rate were studied by growing InAs QDs with various growth rates [26]. The AFM results in Fig. 2.11 show that when the growth rate increases from 0.005 ML/s to 0.4 ML/s, the QD height decreases from about 14 nm to 5 nm, whereas the density increases from 1.2 x 10^9 cm^{-2} to 4.24 x 10^{11} cm^{-2}. This is due to the reduction of diffusion length as the growth rate increase, similar to the case of growth temperature.

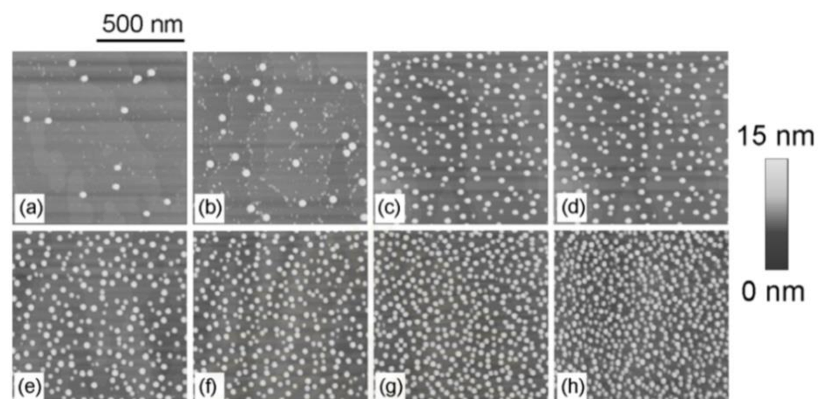

Figure 2.11 AFM images of 1.8-ML InAs QDs fabricated with the InAs growth rates of (a) 0.005 ML/s, (b) 0.008 ML/s, (c) 0.03 ML/s, (d) 0.04 ML/s, (e) 0.06 ML/s, (f) 0.1 ML/s, (g) 0.2 ML/s, and (h) 0.4 ML/s [25]

2.4 The studies of self-assembled NHs

Self-assembled nanoholes (NHs) can be fabricated by various techniques, such as droplet epitaxy and etching. This section will focus on a partial-capping technique, developed by Rudeesun Songmuang (SDRL, 2005) [12]. NHs were found when she studied the evolution of InAs QDs during capping process. The NHs have been used as substrates to fabricate many types of nanostructures, such as nanopropeller QDs, lateral quantum dot molecules, and QDs chains as shown in Fig. 2.12.

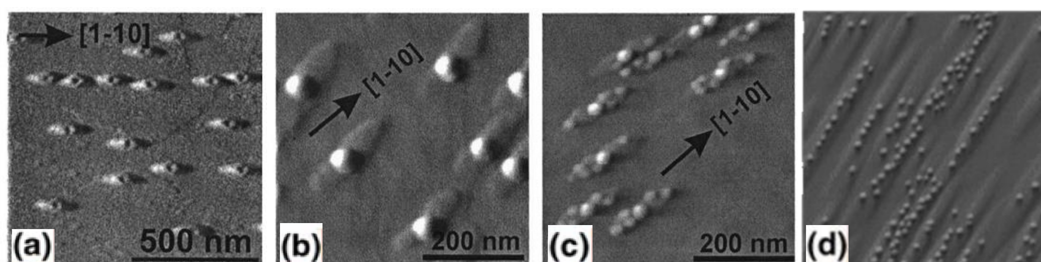

Figure 2.12 AFM images of (a) nanoholes, (b) nanopropellars,(c) quantum dot molecules [27] and (d) quantum dot chains [28].

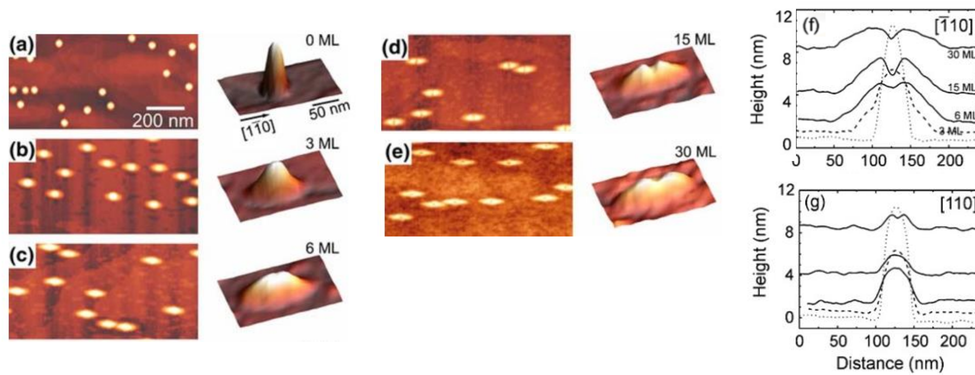

Figure 2.13 AFM images and corresponding oblique 3D views of 1.8-ML InAs QDs overgrown with (a) 0-ML, (b) 3-ML, (c) 6-ML, (d) 15-ML, (e) 30-ML GaAs [29]. Linescans of the nanostructures along (f) [1-10] and (g) [110] directions [30].

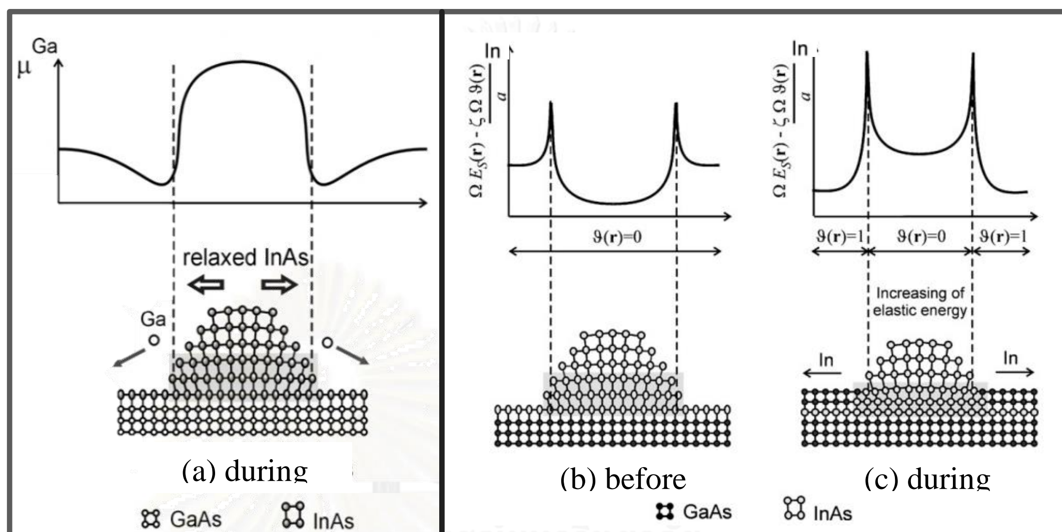

Figure 2.14 Schematic illustrating the effects of thin GaAs capping on (a) Ga local surface strain energy μ and (b)-(c) In elastic energy and wetting chemical potential $\Omega E_s(r)$- $\frac{\zeta\Omega\vartheta(r)}{a}$ [25].

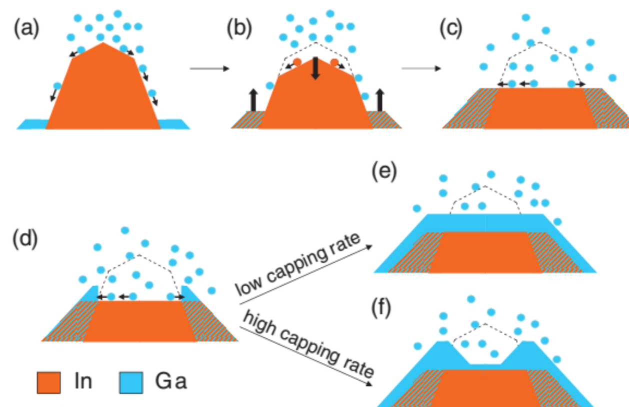

Figure 2.15 Schematic illustrating the evolution from QDs to NHs during GaAs capping process [31].

The partial-cappinp technique described here is based on Songmung (2005), whereas the process and certain growth parameters may change in other experiments. The process starts by the deposition of 1.8-ML InAs with low grow rate (0.01 ML/s) to fabricate large-sized QDs on a GaAs substrate at 500°C. They add 30-s to increases the QD homogeneity. After that the temperature is reduced to 460°C, and then it is waitted for 300 s. Finally, the QDs are covered with a thin layer of GaAs with fast growth rate (0.6 ML/s). GI is not reported in Songmung's works, whereas the GI used by her junior Suraprapapich is 20 s [32].

The evolution of InAs QDs during capping process was studied by varying the capping thickness, in systematical order, from 3 ML to 30 ML. The AFM images and line scans along the two orthogonal directions are shown in Fig. 2.9. After covered by 3 ML, a 11-nm QD collapses and transforms to a 6-nm mound elongated along the [1-10] direction. The mound height decreases with the capping thickness, and interestingly hole is observed when the deposition thickness ≥ 6 ML.

The NH nucleation mechanism can be explained by surface strain energy [25] and kinetic model [31] as follows. Firstly, the surface strain energy of Ga in Fig. 2.14(a) shows the high-energy areas on a QD and the lowest-energy areas around the QD. Therefore, during the deposition, Ga atoms on the QD and nearby the QDs will migrate to the QD edge, as shown in Fig. 2.15(a). Ga accumulation around the QD will compress the QD and change the QDs energy as seen Fig. 2.15(c): the QD energy increases and becomes higher than the surrounding energies. Consequently, In atoms migrate out of the QD, and the QD collapse. In atoms prefer to diffuse in the [1-10] direction, and they intermix with Ga giving rise to InGaAs mound in the [1-10] direction, as shown in Fig. 2.15(b). The process continues such that the QD height decreases but the mound height increases until the QD and mound heights equal, as shown in Fig. 2.15(c). Subsequently, Ga atoms deposited on the QD still migrate out of the QD and originate GaAs ridges, thus a hole as shown in Fig. 2.15(d). After this stage, GaAs will cover the nanostructure, and the hole will remain on the mound if the GaAs is deposited at fast rate, as shown in Fig. 2.15(e).

จุฬาลงกรณ์มหาวิทยาลัย
Chulalongkorn University

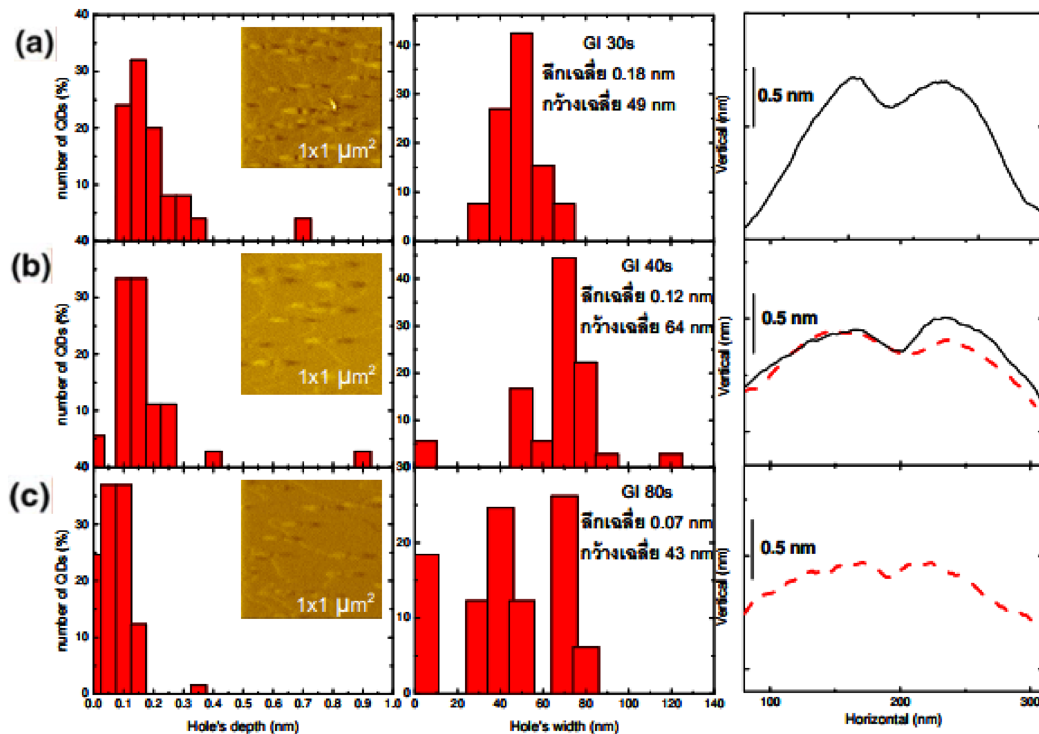

Figure 2.16 AFM images, linescans along [1-10] direction, and corresponding histograms for the depths and widths of the NHs grown with (a) 30-s, (b) 40-s, (c) 80-s GIs [33],

The effects of GI were studied by Patanasemakul (2011) [33]. After the NH fabrication, the processes are hold with three different GIs: 30s, 40s, and 80s. The AFM results in Fig. 2.16 show that when GI increase, the NHs trend to expand in the [1-10] direction, and therefore the height decrease. Also, the depths of NHs decrease from 0.18 nm (30s) to 0.12 nm (40s) and 0.07 nm (80s).

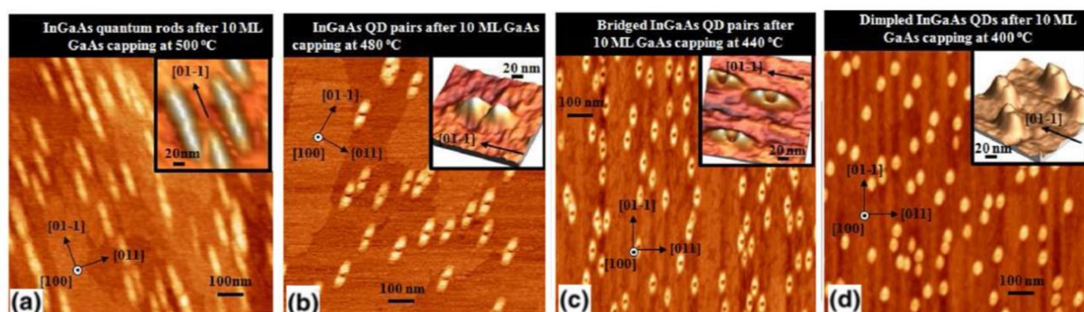

Figure 2.17 AFM images of InAs QDs overgrown with 10-ML GaAs at (a) 500°C, (b) 480°C, (c) 440°C, and (d) 400°C [34].

จุฬาลงกรณ์มหาวิทยาลัย
CHULALONGKORN UNIVERSITY

The effects of capping temperature were studied by Jihoon Lee et al. (2010) [34]. Fig. 2.17 shows the AFM results for the thin GaAs capping at four different temperatures: 500°C, 480°C, 440°C, and 400°C. They found that the capping temperature affects the In diffusion length, especially in the [1-10] direction, and giving rise to the different shapes of nanostructures, as follows. At 500°C, InGaAs quantum rods with the length of 150 nm are nucleated. At 480°C, InGaAs QDs pairs with the length of 125 nm are nucleated. At 440°C, bridged InGaAs QDs pairs with the length of 100 nm are nucleated. At 400°C, dimpled InGaAs QDs are nucleated.

The effects of capping rate were studied by G. Costantiny et al. (2006) [31]. InAs QDs are capped with two Ga rates: 0.6 ML/s and 0.08 ML/s. The AFM results are shown in Fig. 2.18. For the fast capping rate (0.6 ML/s), In atoms spread out in the [1-10] direction, and NHs are observed clearly when the thickness is 15 ML. For the low capping rate (0.08 ML/s), it turn outs that In atoms spread out of QDs further than the previous case due to the longer deposition time, and the holes on top of the mounds are disappear when the thickness is 11 ML.

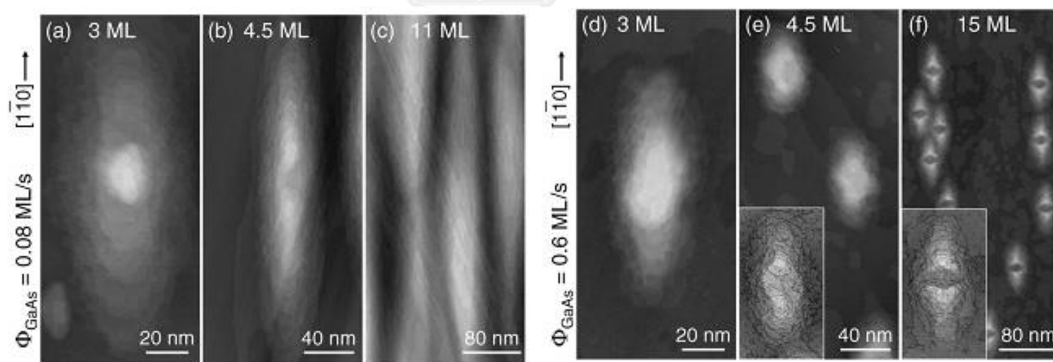

Figure 2.18 AFM images of the nanostructure evolution during GaAs capping at (a)-(c) low (0.08 ML/s) and fast (0.6 ML/s) rates [31]

2.5 The studies of self-assembled QDMs

Self-assembled quantum dot molecules (QDMs) presented in this part are fabricated by a partial-capping-and-regrowth technique (SDRL, 2008). This technique utilizes the NHs as templates and then regrows InAs to create QDMs. The QDM is a group of QDs comprise a big center QD and small satellite QDs. Therefore, PL spectrum from this nanostructure comprises two peaks.

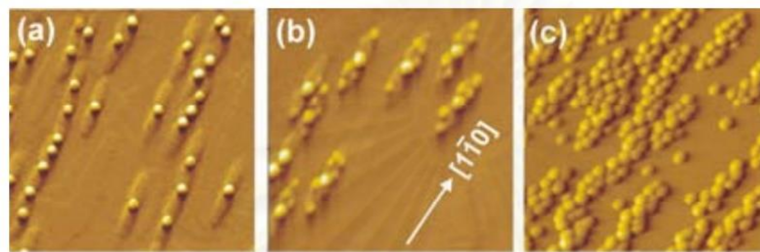

Figure 2.19 AFM images of NHs overgrown with (a) 0.6-ML, (b) 0.9-ML, and (c) 1.2-ML InAs [32]

The nucleation sequence of QDMs was first studied by Suwaree Suraprapapich [32]. NH templates are over-grown by InAs with three different thicknesses: 0.6 ML, 0.9 ML, and 1.2 ML. The AFM results are shown in Fig. 2.19. For 0.6 ML, QDs originate on the middle of NHs which is called nano-propellers (NPs). For 0.9 ML, cQDs in the middle of NHs become larger, and smaller QDs nucleate on propeller's blade. For 1.2 ML, the density of sQDs increases, and it turn out the sizes of cQDs and sQDs are similar due to the cQD-growth saturation. The schematic of nanostructures that develop from QDs to QDMs is shown in Fig. 2.20.

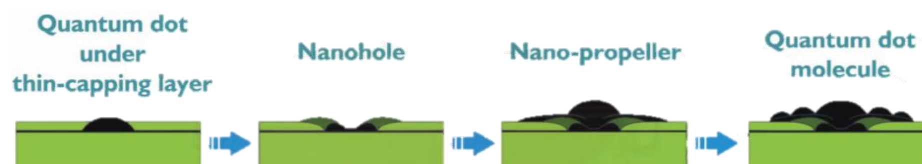

Figure 2.20 Schematic illustrating the evolution from QDs to QDMs through the partial-capping-and-regrowth technique [35].

The length of NPs can affect the number of sQDs per QDM. NPs and QDMs are fabricated at three different temperatures: 470°C, 450°C, and 430°C. The AFM results are shown in Fig. 2.15. They found that when the temperature decrease from 470°C to 450°C, and 430°C, the lengths of NPs also decrease from 275 nm to 215 nm, and 153 nm; consequently after InAs regrowth, the numbers of QDs per QDM decrease from 10-12 dots (470°C) to 6-7 dots (450°C), and 4-5 dots (430°C).

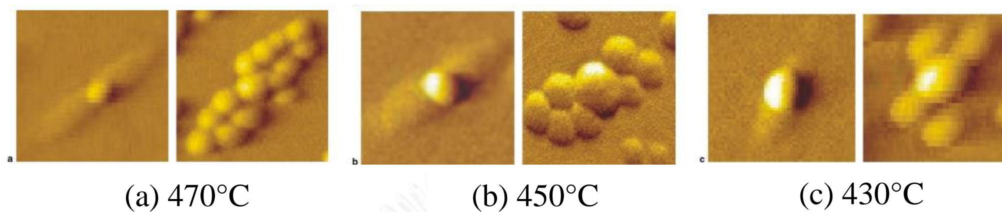

(a) 470°C (b) 450°C (c) 430°C

Figure 2.21 AFM images of (a) NPs and corresponding QDMs grown at (a) 470°C, (b) 450°C, and (c) 430°C. [36]

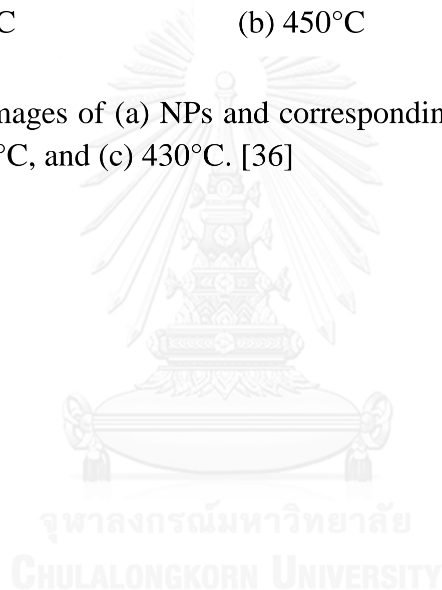
จุฬาลงกรณ์มหาวิทยาลัย
CHULALONGKORN UNIVERSITY

CHAPTER 3
Research methodology

This chapter provides the experimental details from sample fabrication to characterization techniques which are divided into three main sections. The first section discusses about MBE experiment: including the components of RIBER 32P, the applications of RHEED, and sample preparation. The second section presents surface-morphology via AFM technique. The last section presents optical-properties analysis via PL technique.

3.1 Molecular beam epitaxy

3.1.1 RIBER 32P MBE machine

Molecular beam epitaxy (MBE), invented by Bell Telephone Lab in the 1960s, is a crystal growth method with the high accuracy of material control in the order of monolayer. All samples in this study are fabricated via RIBER 32P MBE machine pictured in Fig. 3.1 (a) with schematic diagram in Fig. 3.1 (b). The experiments are conducted under ultra-high vacuum (*UHV*, $<10^{-9}$ Torr) achieved using *ion pump* and *Ti-sublimation pump*, providing the high perfection and low impurity of the crystal structure. The RIBER 32P MBE machine is separated by *gates* into four chambers:

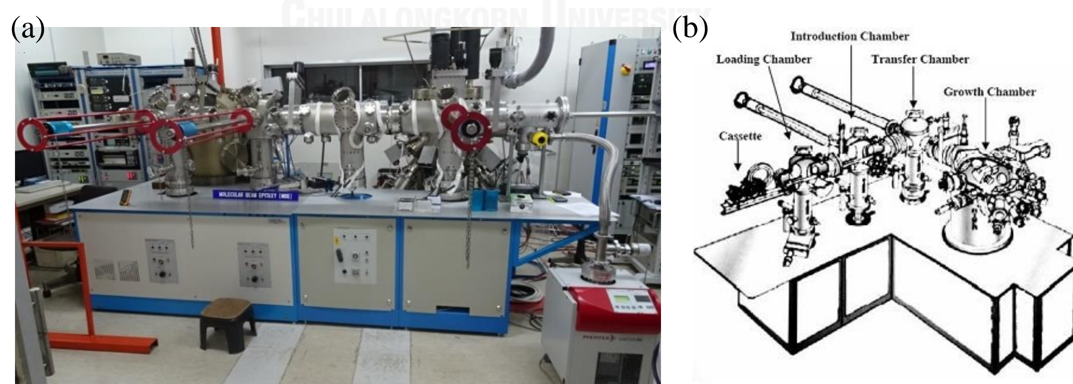

Figure 3.1 (a) RIBER 32P (left) and RIBER Compact 21 (right) solid-source MBE machine at faculty of electrical engineering, Chulalongkorn University. (b) Schematic diagram of RIBER 32P MBE machine [26].

Chulalongkorn University

1. Loading chamber is the first port of entry connected directly to the outer environment. In case of transferring samples out of the machine, it is allowed only after a leakage of pure nitrogen gas until the chamber's pressure is equal to environmental pressure. Conversely, after transferring samples into the machine, the chamber must undergo the serial pumping—namely, *scroll pump, turbo pump, ion pump, and Ti sublimation pump, respectively*—until the chamber's pressure reaches UHV.

2. Introduction chamber is located between the loading chamber described above and the transfer chamber to be described next. The chamber possess an oven which is used for *preheat process*.

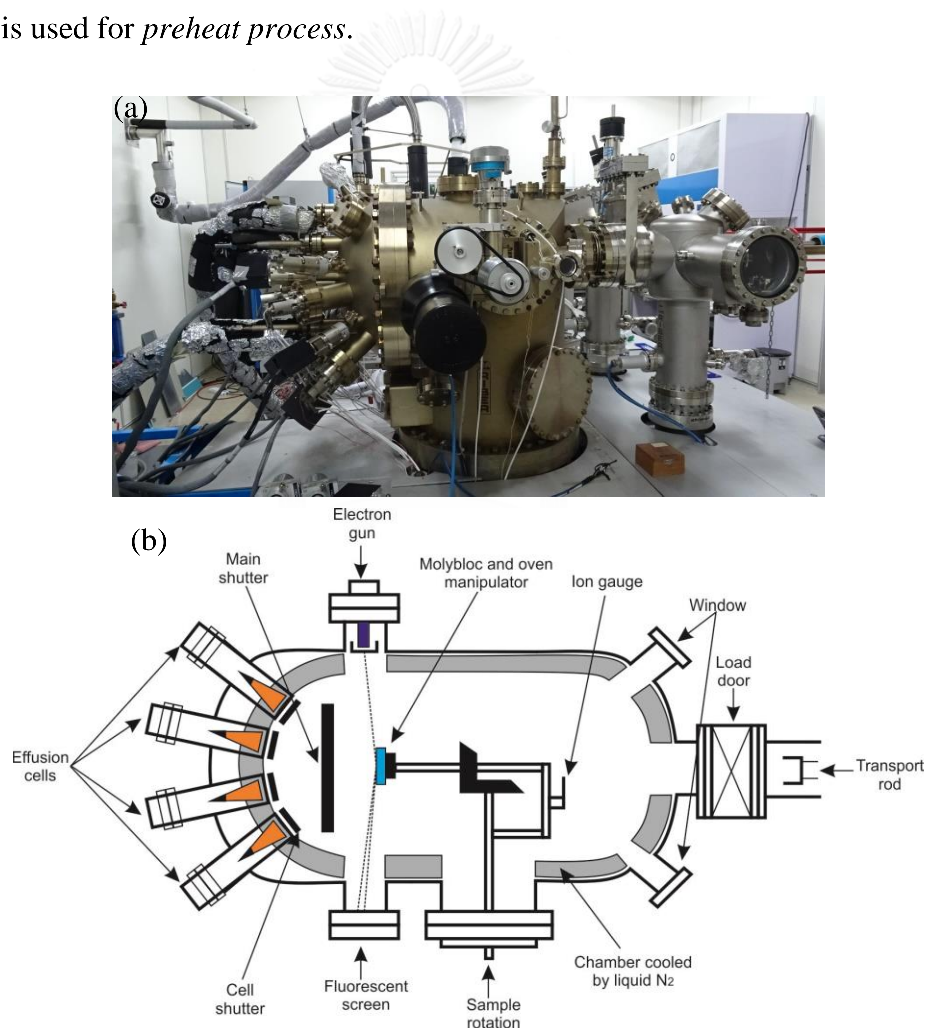

Figure 3.2 (a) Growth chamber of RIBER 32P MBE machine taken from side view. (b) Schematic diagram of growth chamber displayed from top view [37].

3 Transfer chamber is located between the introduction chamber and the growth chamber.

4 Growth chamber is the main part of the machine where MBE experiments are conducted. The chamber comprises many components as shown in Fig. 3.2 (b). A *transport rod* is used to transfer samples between the transfer chamber and the *oven manipulator (OM)*, in the middle of growth chamber. There is an *ion gauge* for flux measurement directly behind OM, and their positions can be rotated for three important purposes: transferring samples, measuring flux, and growing samples. Ultra-pure solid elements—such as In, Ga, Al, As— in separate *effusion cells* are generally heated to standby temperatures of at least 100°C to prevent condensation. During the experiment, molecular beam from each cell is controlled by the *Main shutter* and a related *cell shutter*, while *liquid nitrogen* circulates around the cryoshroud to ensure low pressure and to also serve as thermal isolation between effusion cells. Last but not least, *electron gun* and *fluorescent screen* are installed for real-time and in-situ surface monitoring, called a *refection-high-energy-electron-diffraction (RHEED)* technique which will be described next.

จุฬาลงกรณ์มหาวิทยาลัย
Chulalongkorn University

3.1.2 RHEED

RHEED technique allows user to investigate overall surface morphology during experiments. Fig. 3.3 (a) shows the schematic diagram of RHEED technique. Originated from a 15-kV electron gun, the electron beam is focused on the sample surface with small incident angle ($\theta \sim$ 1-2°). Based on particle-wave duality, due to short de Brogile wavelength of high-energy electrons, electrons behaving like a wave diffract with atomic network on the surface and, finally, reflect on a fluorescent screen as a *diffraction pattern*. Because the pattern is governed by Laue diffraction condition associated with reciprocal lattice of the surface, it can be used as an indicator for surface condition.

Important RHEED diffraction patterns are the streaky pattern in Fig. 3.3(b), the de-oxidation pattern in Fig. 3.3(c), and the spotty pattern in Fig. 3.3(d). The streaky pattern indicates the flat (001)-GaAs surface. The de-oxidation pattern is observed during the removal of native oxide from the surface.The theoretical temperature when this happens is T_{deox} = 580°C. The spotty pattern indicates InAs QDs. Moreover, the transition of RHEED patterns as substrate temperature (T_{OM}) is varied is used to measure the real surface temperature and the deposition rates of Ga and In as follows.

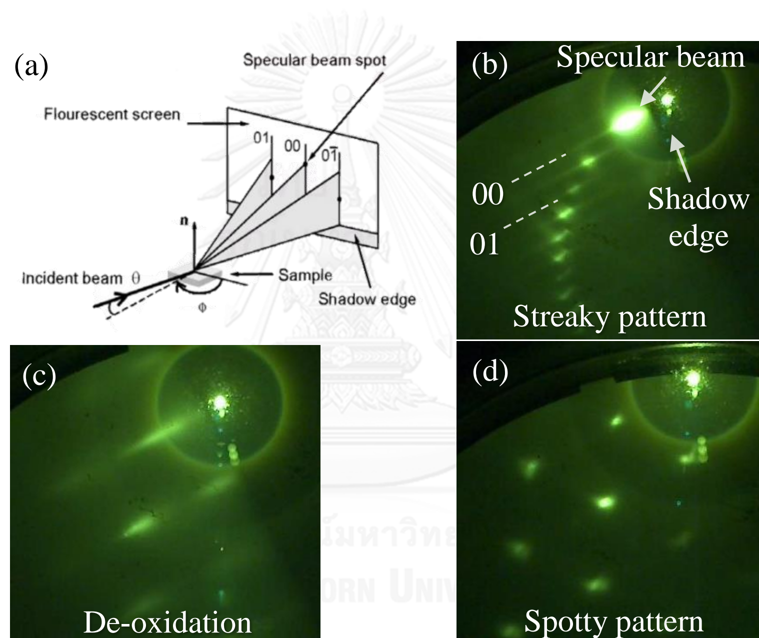

Figure 3.3 (a) Schematic diagram of RHEED technique [25] and examples of diffraction patterns on a fluorescent screen: (b) streaky patter indicating flat surface, (c) de-oxidation pattern, and (d) spotty pattern indicating InAs QDs.

3.1.2.1 Temperature calibration for sample surface

The temperatures of OM and all effusion cells are controlled by Eurotherm's FICS-11 controller. The most important temperature is the surface temperature; its accurate measurement is only way to ensure repeatable, systematic experiments. The displayed temperatures are in fact thermocouple temperatures, not the real temperature of the surface nor the effusion cells. The temperatures thus need to be calibrated in every experiment, especially the surface temperature. A standard surface temperature calibration is carried out for GaAs substrate by observing the RHEED-pattern transition at 500°C [38] using the following procedure.

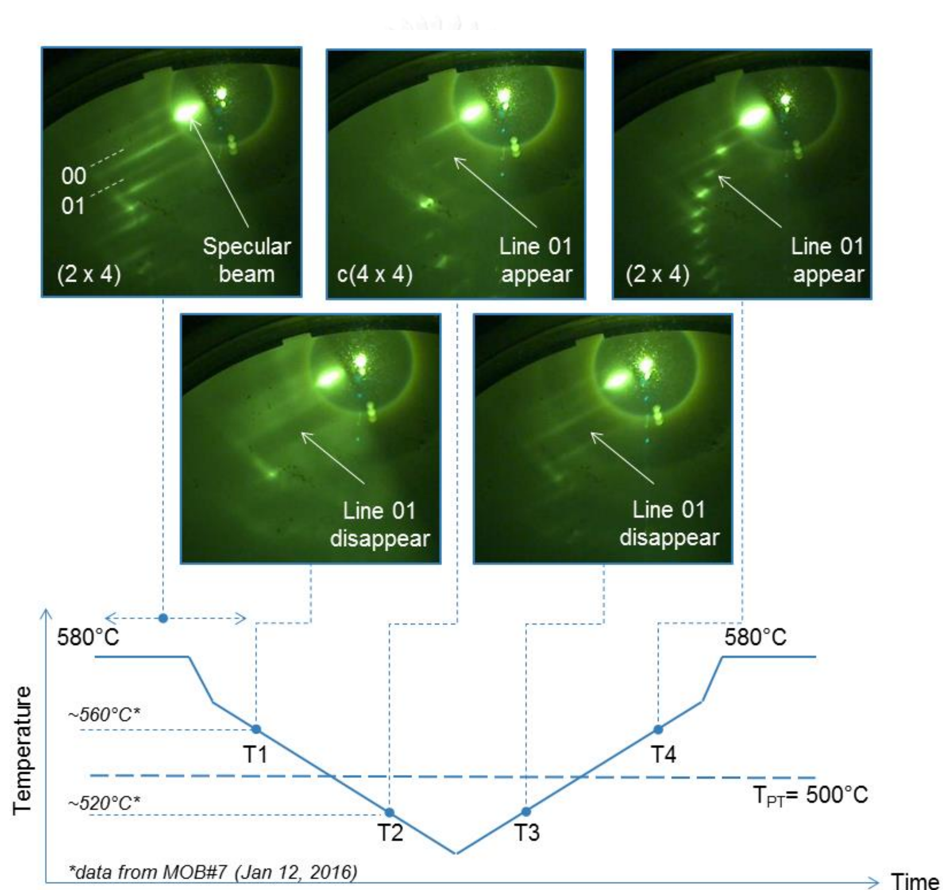

Figure 3.4 Temperature profile of temperature calibration for sample surface and RHEED diffraction patterns relative to four critical points (T1 – T4).

After thermal de-oxidaton at T_{deox}+ 30°C for 20 minutes and a regrowth of 100-nm GaAs, the surface should be flattened and the RHEED pattern should be streaky as shown at T_0 in Fig. 3.4. We stop rotating OM by turning off the DC motor driving the OM, and adjust the OM's angle such that the electron beam impinges the sample in the [1-10] direction. Correct alignment should result in the brightest specular beam. The OM temperature is then ramped down and up according to the profile in Fig. 3.4. The RHEED pattern then cycles between the (2x4) and c(4x4) conditions at four critical points (T1 – T4).

At de-oxidation temperature (580°C, theoretically), the RHEED pattern of flat (001)-GaAs surface under As rich condition is called (2x4) pattern. The pattern consists of several straight lines and important line is at 01, which is located at the third line counting from the specular beam (Fig. 3.4); the line is a reference in the calibration. The temperature is changed as the profile in Fig. 3.4 using fast rate of 30°C /min during 580°C and 550°C, and low rate of 10°C /min for temperature lower than 550°C. Along the process, we register temperatures T1, T2, T3, and T4 when the intensity of the 01line is at minimum (T_1, T_3) and maximum (T_2, T_4). The average of the four temperatures T_{av} is theoretically 500°C.

3.1.2.2 Growth-rate calibration for Ga

By virtue of the real-time RHEED detection, MBE technique enables a crystal growth with slow grow rate and high accuracy. Deposition of Ga on flat GaAs substrate under As-rich condition, generally, reconstructs GaAs layer by layer. The growth thickness in MBE experiments is referred as monolayer (ML), equal to 0.28 nm for GaAs, which can be interpreted from the oscillation of the specular beam. Fig. 3.5 (a) shows schematic surface of GaAs in five different stages (from A to E) during one reconstruction cycle, and the corresponding intensity of RHEED is shown in Fig. 3.5 (b).

Beginning with a perfectly flat surface (A), GaAs deposition roughens the surface (B), so an electron beam disperses on the rough surface giving rise to a dimmer RHEED pattern. The pattern intensity reduces to the lowest point when the thickness is equal to 0.5 ML (C). After that, the intensity starts to increase because it turns out that further deposition re-flattens the surface (D), and the brightest pattern is observed, again, when the thickness is exactly 1 ML (E).

The calibration procedure begins with setting Ga cell and OM to the intended temperatures, while the As and OM shutters remain open to ensure the surface is under an As rich condition. The DC motor is then stopped, and the OM's angle is turned to the position that yields the brightest specular beam position which should be the same as when the sample-surface temperature is calibrated. Next, the Ga shutter is opened and closed for a short time during which a few oscillation cycles are observed and timed in order to determine the growth rate. For example, if we observe RHEED pattern oscillates for 6 cycles in 10 s, the growth rate is 0.6 ML/s. However, durting Ga calibration, the OM is not rotating, we thus cannot create flat GaAs layer thorough out the sample. The contrast between brightest and darkest pattern, therefore, decreases with the time, as shown in Fig. 3.5(c), and consequently we have to re-grow GaAs while OM is rotating to bring back the flat surface.

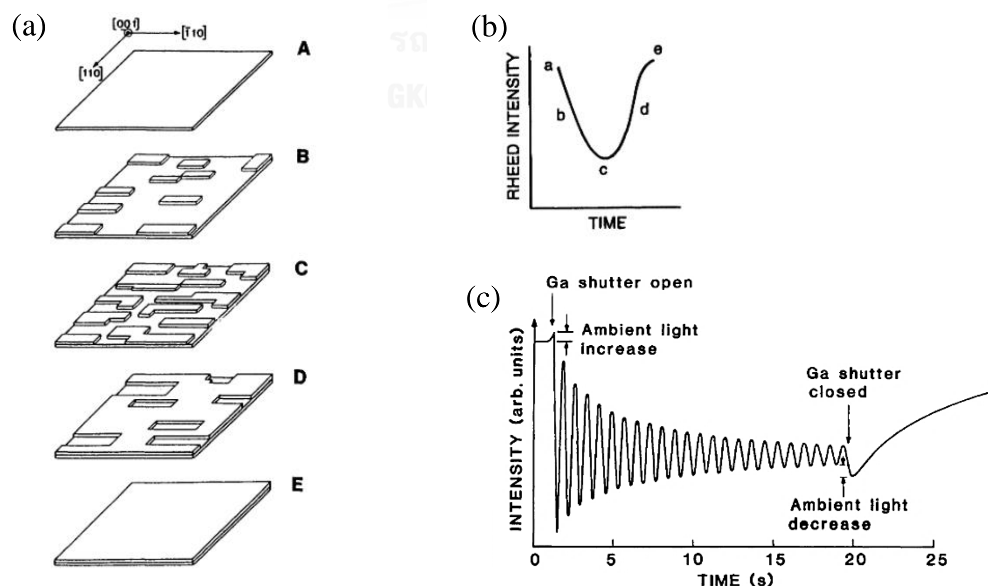

Figure 3.5 (a) Surface reconstruction of 1-ML GaAs and (b) corresponding RHEED intensity from state A to E [39]. (c) RHEED-intensity oscillation during GaAs deposition [40].

3.1.2.2 Growth-rate calibration for indium

A heteroepitaxy of InAs/GaAs introduces strain to the crystal structure which results in the formation of QDs via the SK growth when the deposition of InAs reaches a critical thickness of 1.7 ML, as discussed in Chapter 2. We can exploit this fact and use the transition of RHEED patterns to measure the growth rate of In.

The calibration starts by setting the OM and In cells to the intended temperatures. The In shutter is then opened to deposit InAs onto a rotating GaAs substrate. When the RHEED pattern changes from the streaky to the spotty pattern, it indicates 3D-QD formation, and the In shutter is closed immediately. The operator has to start stopwatch as soon as the In shutter opens and stop the stopwatch when the spotty pattern appears. The InAs growth rate is then calculated by dividing 1.7ML by the time on the stopwatch. For example, if the shutter is opened for 2 minutes and RHEED pattern changes to spotty pattern, the growth rate is ~0.009 ML/s

After the calibration, the OM is ramped up to Tdeox (580°C) in order to desorb the just-grown InAs QDs. Afterward, a 100-nm GaAs layer is deposited in order to bring back a flat surface.

3.1.3 Experimental procedures

3.1.3.1 Conventional sample preparation

Epi-ready (001)-GaAs wafers are used as starting substrates for all samples. After dividing a 2″ wafer into several small pieces, one small piece is selected and mounted on a molybloc using In glue and then transferred to the MBE system. The molybloc with the mounted sample is then loaded in the introduction chamber, then undergoes a 400°C preheat process to eliminate water vapor for one hour. Before the actual growth process begins, In and Ga effusion cells must have been outgassed for 5 minutes at the highest temperatures to be used plus 30°C for the sake of purification. The sample is transferred to the growth chamber and ramped to 300°C. After this process, the shutter of arsenic cell is open and remains open throughout the experiment to ensure the arsenic rich condition which is necessary to prevent arsenic desorption out of the GaAs wafer and thus Ga droplet formation. Afterwards, the temperature is ramped up until a RHEED pattern observed, which is equivalent to

theoretical de-oxidation temperature (T_{deox}, 580°C), and to assure that the native oxide is fully desorbed, it is kept at T_{deox}+ 30°C for 20 minutes. The next step is surface flattening at T_{deox} (580°C) by growing a 200-nm GaAs buffer layer. Haft-way through the buffer layer growth, when the RHEED pattern is sufficiently streaky, a pattern-transition process is carried out as explained earlier. Finally, the rates of In and Ga are calibrated, followed by the growth of another 100-nm GaAs buffer for surface flattening.

3.1.3.2 QDMs on CHPs growth procedure

To study the formation of QDMs on CHPs, we decide to grow three sequential nanostructures: nanoholes (sample A), nanopropellers (sample B), and QDMs (sample C) on CHPs. The cross-sectional schematics of the three nanostructures are displayed in Fig. 3.6, while the temperature profile during sample growth is illustrated in Fig. 3.7. The process begins with CHP fabrication at 500°C. In and Ga beams are simultaneously deposited on the surface at growth rates of 0.05 and 0.2 ML/s, respectively, to create $In_{0.2}Ga_{0.8}As$ 25 nm, which far exceed the critical thickness of CHPs (6 nm). The growth process is held for 25 sec, and then the CHP layer is covered by 6-nm GaAs to decrease the surface strain. The following nanohole-fabrication process was proposed and optimised by Rudeesun Songmuang [25]. At 490°C, conventional 1.7-ML InAs QDs are grown at a low rate (0.01 ML/s). The In shutter is closed instantly when the spotty RHEED pattern appears. Then, we interrupt the growth process for 30 s to improve QD homogeneity [21]. The temperature is then set to 460°C with a nescessary 3-minutes delays to maintain the shape of QDs. Next, a crucial step to create nanoholes, is to deposit onto InAs QDs a thin (10 ML) GaAs at a fast rate (0.9 ML/s). After a 15-s growth interrupt (GI), nanostructures on the surface are frozen by stepping the temperature down to 100°C immediately, finishing the growth procedure for sample A. In the case of nanopropellers (sample B) and QDMs (sample C), instead of dropping the temperature down to 100°C, we regrow InAs with 1.0 ML and 1.5 ML on the nanoholes, respectively. This is followed by a 30-s GI before stepping down to 100°C. The surface morphologies of samples A, B, and C are subsequently investigated via AFM technique. Furthermore, another sample with an

identical structure to sample C is grown, but the nanostructures are capped by 100 nm GaAs to examine the optical properties via PL technique.

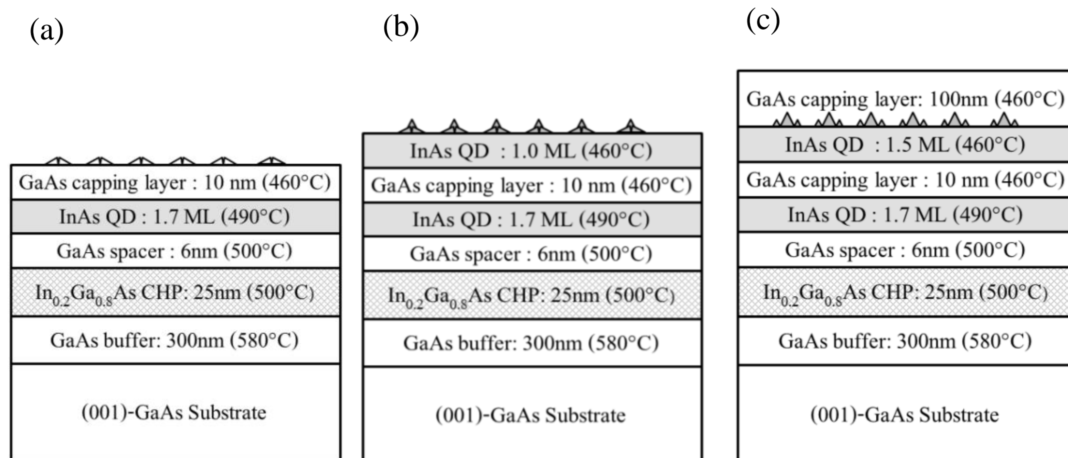

Figure 3.6 Schematic cross-sectional diagrams of samples (a) A—nanoholes, (b) B—nanopropellers, and (c) C—QDMs on CHPs.

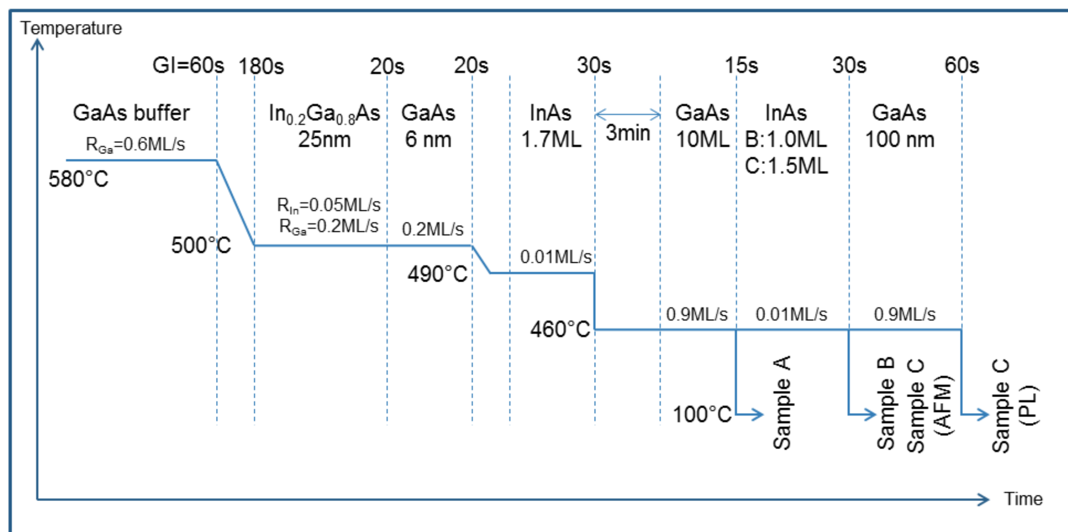

Figure 3.7 A temperature profile of growth procedures for samples A, B, and C.

3.2 Atomic Force Microscopy

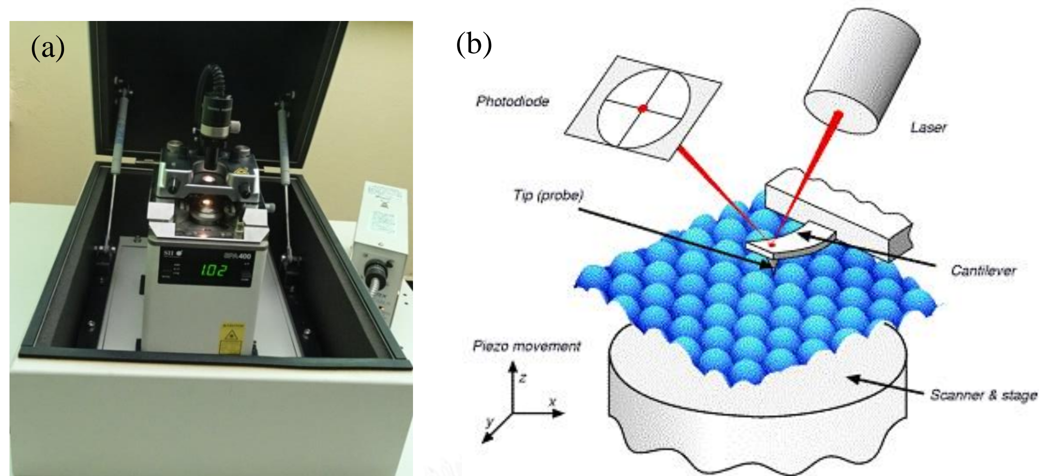

Figure 3.8 AFM characterization (a) picture of Seiko SPA-400 at SDRL and (b) schematic diagram describing the operating principle [41].

Atomic force microscopy (AFM) is a widely used technique for ex-situ surface-morphology investigation with an accuracy in the vertical axis in the order of Ångström. The schematic diagram for AFM components is shown in Fig. 3.8(a). On the *cantilever*, there is a small sharp *tip* and reflective surface on the other side. The sample holder is placed on the *piezoelectric scanner*, while the *laser* and *photodiode* are used to detect the defection of the cantilever. When the tip is moved near the surface, the interaction between the tip and sample surface will bend the cantilever and results in the varying light intensity output from the photodiode. The data are analyzed for the height of this position. Next, piezoelectric scanner will move to another area to measure the height until the scanning covers all the intend area. All data will be collected, analyzed and displayed in the picture of surface morphology.

3.3 Photoluminescence

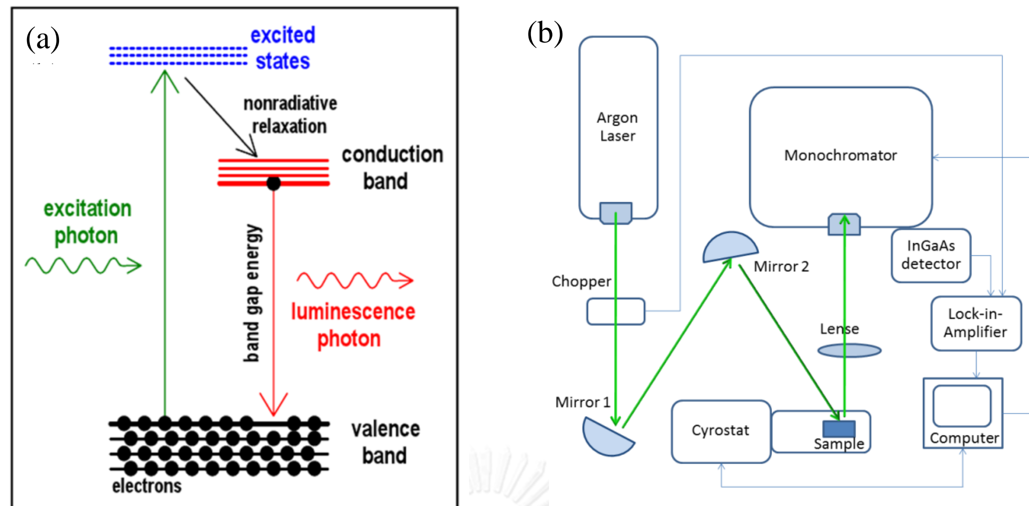

Figure 3.9 (a) A schematic diagram of a PL phenomenon in semiconductor [42]. (b) Components and setup for a PL experiment.

Photoluminescence (PL) is a phenomenon when any matter emits light after absorbing photons. Fig. 3.9(a) shows PL in a semiconductor crystal system which has band gap energy E_g. When light with energy greater than E_g is shined on the surface of a semiconductor, electrons in the valance band will absorb photons and be excited across the band gap to the higher energy levels, in the conduction band. After that, electrons lose their energy to the crystal via phonon emission and consequently move down to the edge of the conduction band in a process called nonradiative relaxation. Finally, electrons will drop to the edge of valence band and emit photons with frequency $f = E_g / h$ when h is the Plank's constant. Because the frequency of emitted photons is associated with the band gap energy, PL is a widely used method for nondestructive testing of semiconductors.

In this thesis, PL technique is used to observe the optical properties of nanostructures and the results will be analyzed with the morphological results from AFM. The optical alignment for a PL experimental setup is shown in Fig. 3.9(b). The experiment begins with loading the *sample* of interest into a variable temperature *Cryostat*. Normally, the temperature is kept as low as possible (about 20 K) to avoid the thermal excitation which can destroy the quantum confinement and lower optical output signal. *Argonion laser* is used as an exciter with the wavelength of 514.5 nm

(green). A *chopper*, similar in structure to a rotating fan, is used to transform laser signal from continuous to discrete, which has high noise immunity. After excited by the laser, the sample emits photons; subsequently, they are collected by *lenses* and transmitted to a *monochromator*. Inside the monochromator, there are gratings that can separate each signal wavelength to the different angle. By controlling the angle of the grating, the interested wavelength can be selected; its power is then measured by an *InGaAs detector*, transforming the optical signal into an electrical signal. *Lock-in amplifier* then amplifies the electrical signal at the chopper frequency. This phase sensitivity detection (PSD) increases the signal-to-noise ratio. The results are then plotted with energy (eV) in the horizontal scale and PL intensity (arbitrary unit, a.u.) in the vertical scale.

จุฬาลงกรณ์มหาวิทยาลัย
Chulalongkorn University

CHAPTER 4
Experimental results and discussion

In recent years, *quantum dots (QDs)* on *cross-hatch patterns (CHPs)* and *quantum dot molecules (QDMs)* nanostructures have become ones of the main research streams in *Semiconductor Device Research Laboratory (SDRL)* with the prospect for fabricating broadband near-infrared materials. Both nanostructures have been studied intensively and consistently by several people [26, 32, 33, 35, 43-45]. The subjects of studies include the characteristics, nucleation mechanism, and manipulation by varying growth parameters. Previously, the idea for a combination of QDs and CHPs has been proposed and studied. In this chapter, we extend the studies and focus on the effects of CHP templates on QDMs. The chapter is divided into three sections. The first section reviews the characteristics and nucleation of QDs on CHPs. The second section presents the evolution of nanostructures on CHPs: from *nanoholes (NHs)* to QDMs. The last section discusses the optical characteristic of QDMs on CHPs.

4.1 Review on the characteristics and nucleation of QDs on CHPs

Conventional InAs QDs are the nanostructures forming on GaAs surfaces due to strain relaxation via the Stranski-Krastanow mode. The QDs randomly distribute on the surfaces, whereas the sizes are normally uniform as a results of the strain uniformity. When CHPs are used as a virtual substrate, they introduce dislocations and modify the strain fields of the surface. As a result, deposited QDs are guided by these dislocations and exhibit variations in size and shape. Fig. 4.1 shows (a) the schematic cross-section and (b) the corresponding AFM image of QDs grown on CHPs studied by Thitipong Chokamnui (2013) [43]. This sample is similar to the structures of interest to this work which will be described later. It should be mentioned here that the differences are twofold: the GaAs spacer thickness changes from 10 to 6 nm, and the QDs growth temperature changes from 500°C to 490°C.

The AFM image in Fig. 4.1(b) shows aligned QDs as guided by orthogonal [1-10] and [110] misfit dislocation (MD) lines, as well as QDs randomly nucleate on flat areas. The number of [1-10] MD lines is far greater than those of [110] MD lines. Moreover, QDs on [1-10] MD lines have higher density than those on [1-10] MD lines and flat areas. The approximate dimensions of QDs in various locations are summarized in table 4.1, and it show that the QD heights on MD lines are greater than those on flat areas, especially on [1-10] MD lines where the size is doubled. These characteristics of QDs on CHPs can be explained by asymmetric GaAs crystal structure in the orthogonal [110] and [1-10] directions, the MD strain field, and atomic migration during the QDs formation as follows.

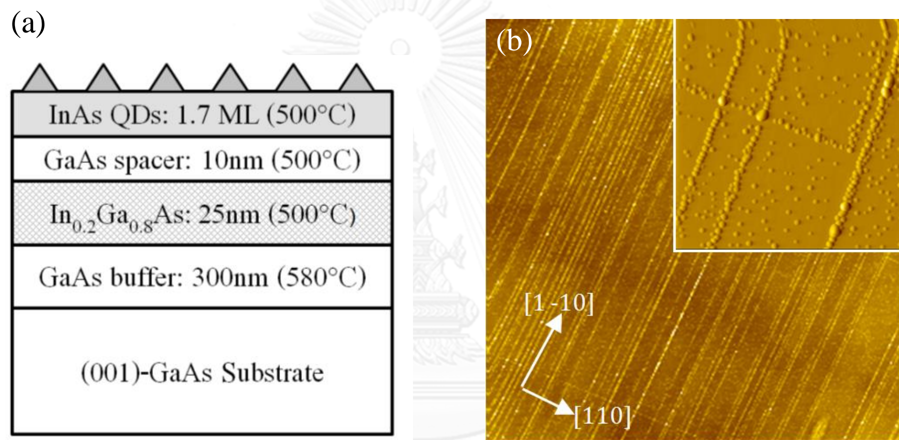

Figure 4.1 (a) Schematic cross-sectional diagram of QDs on CHPs studied by Chokamnui (2013). (b) 10 × 10 μm^2 AFM image of the sample with an 2 × 2 μm^2 inset magnified around the cross sections [43].

Table 4.1 Average dimensions of QDs on flat areas and the two orthogonal MD lines obtained from the AFM image in figure 4.1(b) [44].

	Height (nm)	Length[1-10], L (nm)	Aspect ratio (L/W)
MD [1-10]	6.0	40	1.36
MD [110]	4.5	30	1.2
Flat areas	3.0	25	1.0

As a heteroepitaxy, depositing an $In_{0.2}Ga_{0.8}As$ layer on a GaAs substrate will incorporate misfit strains into the crystal structure. The crucial point is when the deposition reaches a critical thickness (theoretically 6 nm for $In_{0.2}Ga_{0.8}As$/GaAs), a strain relaxation occurs, and it generates *threading dislocations (TDs)* piercing from the intersection through the $In_{0.2}Ga_{0.8}As$ layer. The TDs, subsequently, glide through the surface along [110] and [1-10] directions, leaving surface steps (so-called *misfit dislocations, MDs*); therefore, a plain surface transforms to CHPs. The MD strain fields are asymmetric: it is greater along the [1-10] direction. As a result, the nucleation sequence of QDs is as follow: [1-10] MDs, [110] MDs, and flat surfaces. The sizes of QDs directly correlate with QD nucleation sequence [45]. Furthermore, the strain fields influence the QD shapes (aspect ratio). As seen in table 4.1, the results show that QDs on MDs are slightly elongated along the [1-10] direction, in contrast to typical circular QDs on the flat areas. This phenomenon is prominent in the case of vertical stacked QDs grown of CHP where the polarized optical properties can be expected [44]. From previous discussions, we will see that the MD strain field is a key factor that governs the behaviors of QDs. Therefore, it is worthwhile to investigate the strain field origin in order to understand the CHP effects on QDs thoroughly.

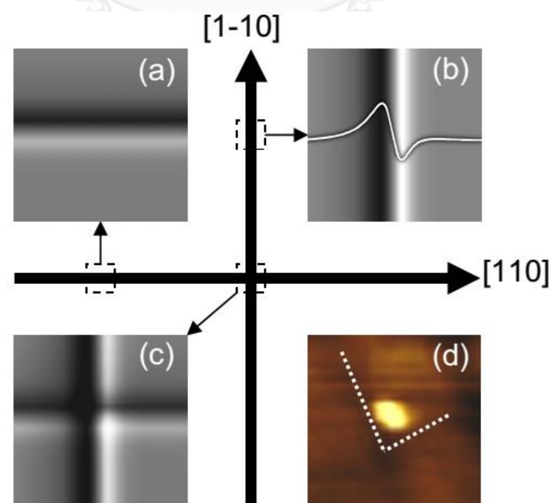

Figure 4.2 Two-dimensional simulated strain distributions of (a) [110] and (b) [1-10] MDs. (c) Combined strain distribution at the cross section. (d) 200 × 200 nm^2 AFM image of a QD on the cross section with dash lines guiding the orthogonal dislocation lines [46].

A simple model to describe the strain-field characteristics is based on a linear superposition of stress distributions from each MD [46]. According to the above discussion, surface steps (or MDs) are a result of strain relaxation; however, it not only leaves high strain along MDs, but it also modifies surface stress. In fact, a MD line is composed of compressive stress on one side and tensile stress on the other. Because the lattice constant of InAs is greater than that of GaAs, InAs QDs prefer to nucleate on the tensile-stress areas. Fig. 4.2(b) shows one-dimensional stress distribution corresponding to [1-10] MDs where the bright and dark colors correlate with the high and low tensile-stress areas, respectively. In other words, the probability of QD nucleation increases with the brightness. The stress distribution of a MD along [110] is also displayed in Fig. 4.2(a) with less brightness tone. For the intersection, the strain distribution seen in Fig. 4.2(c) simply derives from a linear combination of the two orthogonal-MD stresses.

Fig. 4.3 shows a model application where a simulated strain field (Fig. 4.3(b)) is superimposed on a real sample surface (Fig. 4.3(a)). The results are consistent with the prior assumption: the densities of QDs on bright areas are higher than those on dark areas. Interestingly, the brightest and darkest spots are on the intersection (Fig. 4.3(b)). This means that the deposited In atoms will migrate and develop QDs firstly on one side of intersection, while the other side will be the last to develop QDs. Therefore, the tallest QDs are found on the intersection, theoretically. In addition, it is discovered that QDs prefer to form on the flat areas (gray color) rather than the MD compressive sides (dark color).

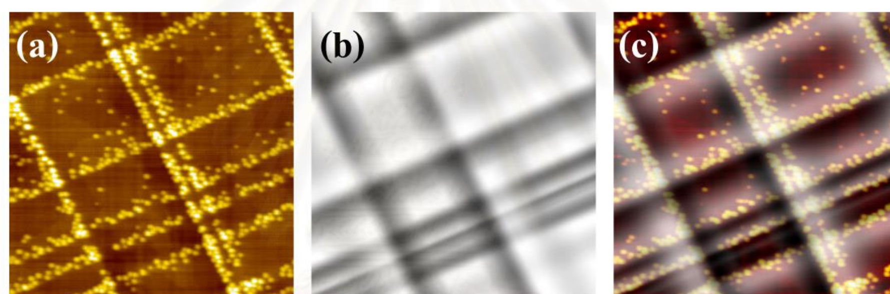

Figure 4.3 (a) $2 \times 2\ \mu m^2$ AFM image of InAs QDs on CHPs. (b) Corresponding simulated strain distribution. (c) Overlapped image of the AFM image and the strain distribution [45].

4.2 The evolution of QDMs on CHPs

InAs QDMs are nanostructures fabricated via the partial-capping-and-regrowth technique, as discussed in Chapter 2. In this section, we are going to analyze the morphology of a series of three samples (A, B, and C) and discuss about the evolution of QDMs on CHPs. Every sample is grown on identical CHP virtual substrates: GaAs substrate overgrown with 25-nm $In_{0.2}Ga_{0.8}As$ and followed by a 6-nm GaAs spacer. For sample A with schematic cross-section in Fig. 3.6(a), NHs are formed as a result of growing 1.7-ML InAs QDs on CHPs and covering the QDs with a 10-ML GaAs layer. For sample B with schematic cross-section in Fig. 3.6(b), nanopropellers (NPs) are formed as a result of growing 1.0-ML InAs on the NHs. For sample C with schematic cross-section in Fig. 3.6(c), QDMs are formed as a result of growing 1.5-ML InAs on the NHs.

Fig. 4.4 shows AFM images of 10 × 10 μm^2 and small insets magnifying around the intersections of the three samples. The shapes and sizes of nanostructures in the three samples differ significantly in various locations. In the case of sample A, it is seen clearly that primary QDs on MDs do not transform into uniform NHs, like those on flat surfaces. Moreover, the morphologies of nanostructures on [1-10] and [110] MDs are dissimilar. The subsequent InAs regrowth on this sample as a template provides high variations in QDs as seen in Figs. 4.4(b) and (c). The following sub-sections further discuss detailed morphologies of the three different locations: (1) flat areas, (2) [110] MD lines, and (3) [1-10] MD lines.

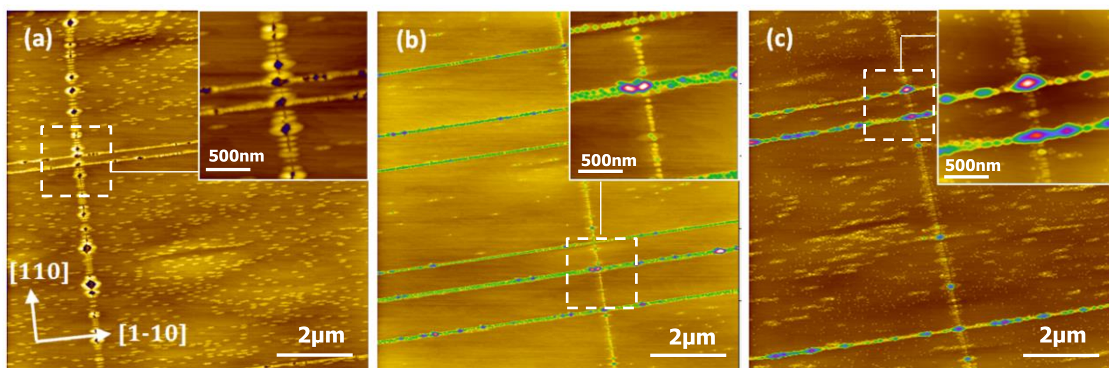

Figure 4.4 10 × 10 μm^2 AFM images with 2 × 2 μm^2 insets magnifing around the cross sections of (a) sample A, (b) sample B, and (c) sample C.

4.2.1 Flat surfaces

On the flat surfaces, the strain distribution is uniform; the evolution from NHs to QDMs is, as expected, the same as those grown on a flat GaAs substrate. The discussions on NHs and QDMs in detail for the characteristics and nucleation, including strain field and growth-parameter variation, are presented in Chapter 2. The AFM images and oblique 3D views of nanostructures found on flat surfaces for the three samples are shown in Figs. 4.5(a)-(c). Also, the nanostructure shapes and sizes in each sample are presented by linescans in Figs. 4.5(d)-(f).

Sample A. Nanostructures observed on the flat surfaces in Fig. 4.5(a) are camel-like shapes elongated along the [1-10] direction, defined as *nanoholes (NHs)*. In fact, an actual nanohole is on the top of a mound, but we will call this structure a *NH* for the sake of clarity and ease of comprehension. From the linescan in Fig. 4.5(d), the dimensions of a representative NH are as follows: the width and height of the mound are roughly 275 nm and 1.5 nm, while the width and depth of the actual nanohole are 70 nm and 0.3 nm, respectively.

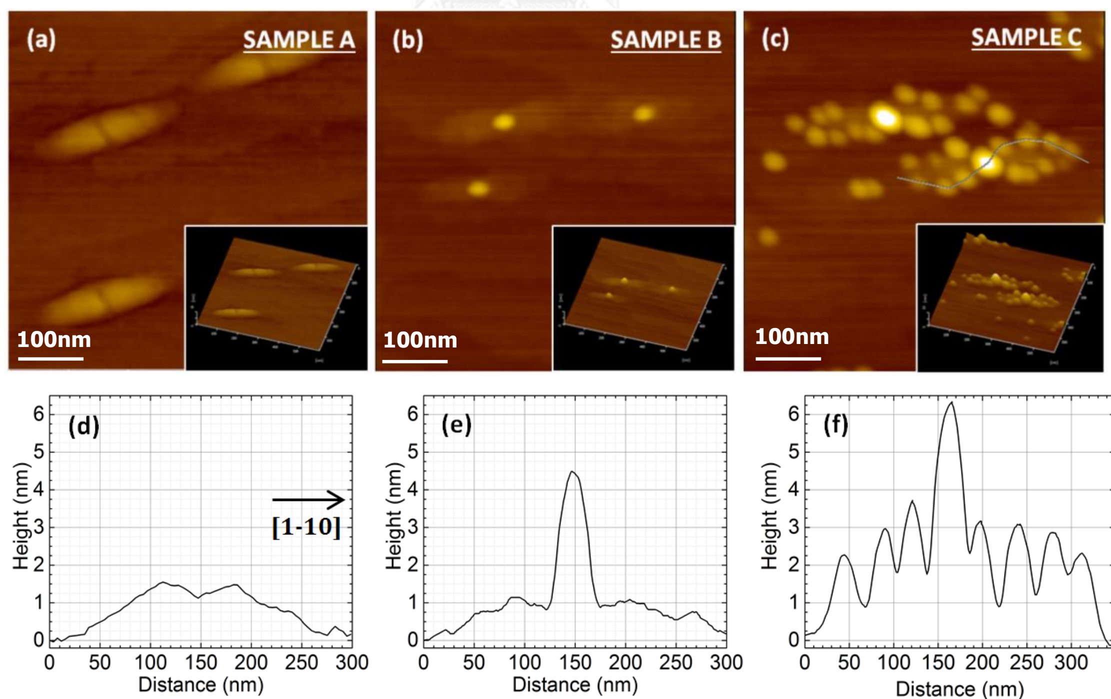

Figure 4.5 600×600 nm^2 AFM images inserted with small oblique 3D views of (a) sample A, (b) sample B, and (c) sample C. Linescans along the [1-10] direction of a typical (d) NH from sample A and (e) NP from sample B. (f) Linescan of QDM along given line in figure 4.5(c).

The following is a brief explanation on the nucleation mechanisms of NHs according to Rudeesun Songmuang [25]. At the primary stage, In atoms prefer to dwell on QDs where the chemical potential is lower than the surrounding, due to strain relaxation via S-K mode. Once Ga atoms are deposited on the top of QDs, they tend to move out of QDs on account of high strain, and begin to mount up around the QDs. The QDs are subsequently compressed so that their chemical potentials are higher than the surrounding. As a result, In atoms migrate out of the QDs leaving *holes* in the middle. In atoms spread out, particularly in the preferential [1-10] direction, and intermix with GaAs, thus giving rise to *mounds* elongated along the [1-10] direction.

Sample B. Regrowth of 1.0-ML InAs creates a single QD on the top of a NH as shown in the AFM image of Fig. 4.5(b). This nanostructure is defined as *nanopropeller (NP)*, as inspired by their shapes. The linescan in Fig. 4.5(e) reveals that the width and height of a typical QD are 45 nm and 4.2 nm, respectively, whereas the corresponding dimensions for a mound are 300 nm and 1 nm. It should be noted that the surface level is a reference point for height measurement, which means that the real height of the QD is around 3.2 nm.

Sample C. Regrowth of 1.5-ML InAs creates additional small QDs around the previous big QD. The nanostructure is defined as *quantum dot molecule (QDM),* where a big *center quantum dot (cQD)* is surrounded by several small *satellite quantum dots (sQDs).* In order to meaningfully compare the shape and size of a cQD and sQDs in the same QDM ensemble, a curved linescan along the path in Fig. 4.5(c) is shown in Fig. 4.5(f). The width and height of the cQD are 50 nm and 6 nm, while the corresponding values for sQDs vary between 30-70 nm and 2-3.5 nm, respectively. In addition, due to the low inter-QD distances, PL measurements from this type of nanostructure should exhibit a carrier-migration behavior [33]. Besides the QDMs, there exist stand-alone *normal QDs (nQDs)* on the flat surfaces, as seen in Fig. 4.6(a). The fact that these nQDs nucleate despite the In deposition of merely 1.5 ML, lower than the critical thickness of 1.7 ML on flat GaAs surfaces, indicates the effects of accumulated strain form the underlying InAs wetting layer and the CHPs.

จุฬาลงกรณ์มหาวิทยาลัย
Chulalongkorn University

. For statistical data analysis, QD height histograms extracted from the 2 × 2 μm^2 AFM (Fig. 4.6(a)) are presented in Fig. 4.6(b) where the QDs are categorized into three groups: cQD, sQD, and nQD. The mean heights in decreasing order are 6.5 nm for cQDs, 3 nm for sQDs, and 2.5 nm for nQDs. The difference in the average heights implies the following nucleation sequence: cQDs, sQDs, and nQDs. Full width at haft maxima (FWHM) of cQDs, sQDs, and nQDs are 1 nm, 1.4 nm, and 1.2 nm, respectively. The number of sQDs per one QDM varies between 10 and 18 dots.

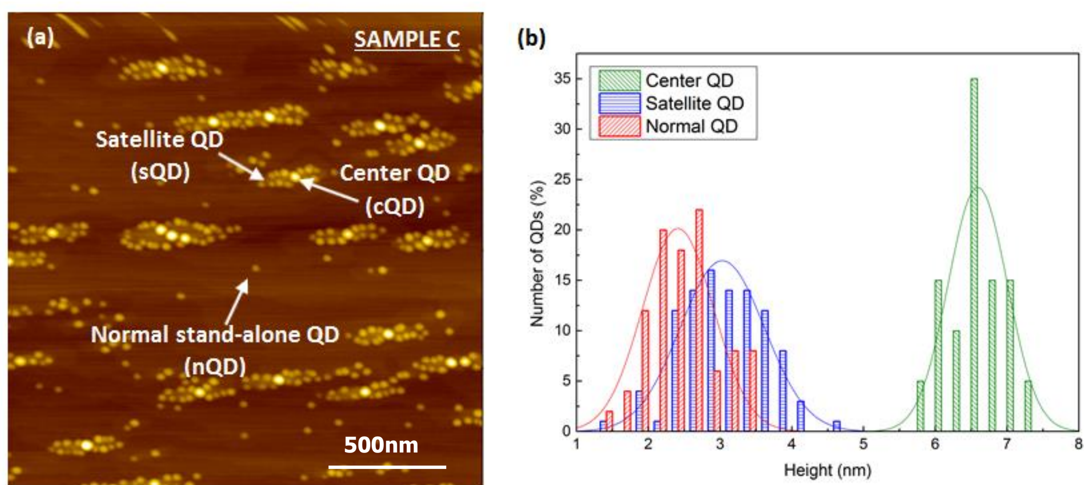

Figure 4.6 (a) 2 × 2 μm^2 AFM image of nQDs and QDMs on a flat surface of sample C. (b) Corresponding QD height histograms.

จุฬาลงกรณ์มหาวิทยาลัย
CHULALONGKORN UNIVERSITY

4.2.2 [110] MD lines

On [110] MD lines, the strain is higher than flat surfaces; therefore, the primary QDs are larger than those on flat areas. The difference in QD sizes influences the NH shape and dimension, as well as the subsequent NPs and QDMs [33]. Another unique MD feature is the asymmetric stress, as explained in Section 4.1; this fact should affect the symmetry of [1-10]-elongated nanostructures. In Fig. 4.7, the 2 × 2 μm^2 AFM images (upper parts) and oblique 3D images (lower parts) show the surface morphologies around [110] MD lines of the three samples.

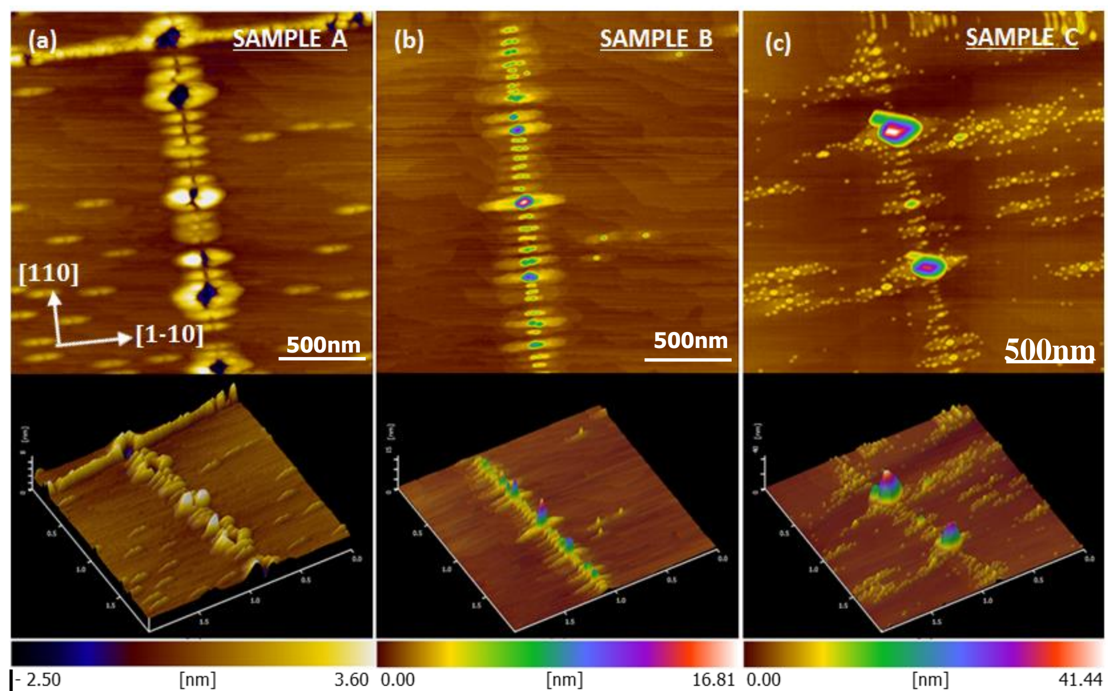

Figure 4.7 2 × 2 μm^2 AFM images (upper panels) and oblique 3D views (lower panels) along [110] MD lines of sample (a) A, (b) B, and (c) C.

The nanostructures on [110] MD exhibit a significant variation. Although, the MD strain field transforms certain nanostructure into the large dimensions. They share a common feature with those on flat surfaces. A quick analysis shows the deepest NH (Fig. 4.7(a)) around 2.5 nm below the surface and the tallest QD (Fig. 4.7(c)) around 40 nm above the surface. Furthermore, it is discovered that certain NHs develop to atypical nanostructures, in comparison to those on flat areas: for example, the NHs that are occupied by 2-3 QDs in sample B (Fig. 4.7(b)) and a NH with obscured sQD

in sample C (Fig. 4.7(c)). Significant variations in morphologies necessitate further, more detailed, analyses as follows.

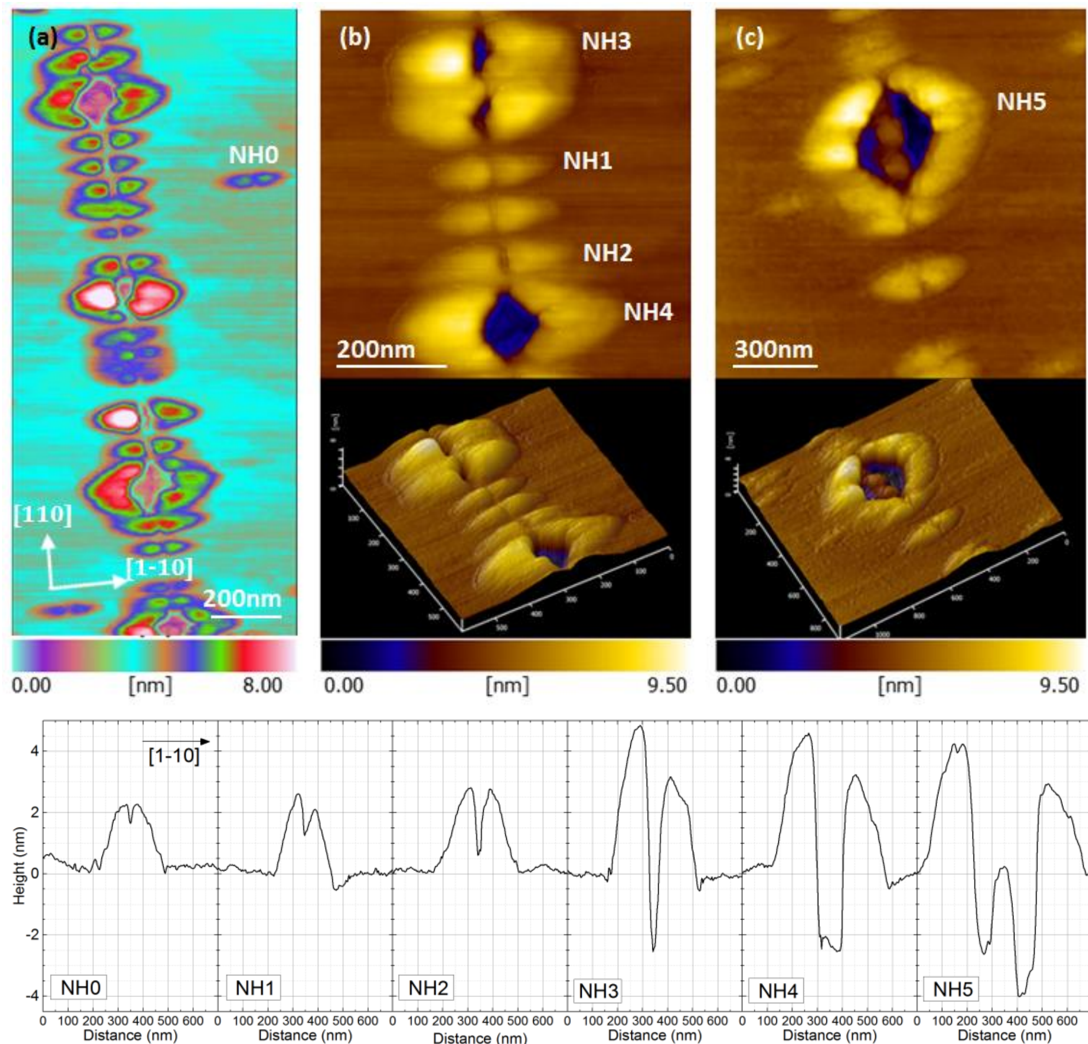

Figure 4.8 (a) 0.8 × 1.6 μm^2 AFM image at a [110] MD line from sample A. (b)-(c) Close-up AFM images and oblique 3D views from two different locations. (d) Linscans of NHs on flat surface (NH0) and a [110] MD line (NH1 - NH5).

Table 4.2 The average dimensions of representative NHs (NH0 – NH5) from the AFM images in Figs 4.8 (b) and (c).

	Dimensions (nm)	NH0	NH1	NH2	NH3	NH4	NH5
Mound	Height	2.3	2.6	2.7	4.8	4.5	4.2
	Δ height	< 0.1	0.6	< 0.1	1.6	1.3	1.3
	[1-10] width	270	240	350	380	480	670
Hole	Depth	0.6	1.2	2.0	7.3	7.0	8.2
	[1-10] width	55	70	95	120	200	350
	[110] width	55	50	60	85	145	340

Sample A. The AFM image in Fig. 4.8(a) is illustrated in a high-contrast color height scale in order to observe the NH shapes of NHs in details. The results show that many NHs are asymmetric in heights: mounds on the left hand side tend to be higher than mounds on the right hand side. This can be simply explained as follows. During the GaAs capping, In atoms generally diffuse out of InAs QDs, and resulting in mounds elongated along the [1-10] direction. Because In atoms prefer to migrate to the tensile area (left hand side), with respect to the compressive area (right hand side), the diffusion rates and subsequent re-crystallization rates in the two directions are different, and finally leaving asymmetric NHs.

Figs. 4.8(b) and (c) are close-up AFM images with oblique 3D images of selected areas where the NH shapes exhibit large deviation. Five NHs (NH1 – NH5) are selected in ascending size order, and their linescans are show in Fig. 4.8(d). A linescan of a typical NH on the flat area (NH0) serves as a reference. The dimensions of all NHs are measured and presented in table 4.2.

NH1 is similar to NH0, except the deeper hole of 1.2 nm and the mound-height offset of 0.6 nm. For the larger NHs, both hole and mound tend to expand simultaneously. For example, when mounds broaden from 240 nm (NH1) to 350 nm (NH2) and 380 nm (NH3), the corresponding holes broaden from 70 nm (NH1) to 95 nm (NH2) and 120 nm (NH3). This trend is simply the results of the conservation of mass: the more In atoms leave QDs (and create a larger hole), the more In atoms are left on the surface (and create a larger mound). It should be noted that all the hole depths reported in Table 4.2 are measured from the mound tops to the hole bottoms. This means the hole depths with respect to the flat surface are obtained by subtracting the hole depths with the mound height in Table 4.2. Interestingly, the depth of NH3 with respect to the flat surface is 2.5 nm (7.3 nm – 4.8 nm), which corresponds to the GaAs capping thickness of 10-ML (2.8 nm). This indicates a high In diffusion rate, but low Ga deposition rate due to the effect of MD strain field.

An interesting result comes with NH4 where the large hole transforms to a remarkable *diamond shape* (Fig. 4.8(b)). The hole widths span 200 nm and 145 nm in the [1-10] and [110] directions, respectively, while the depth of NH, with respect to the flat surface, is 2.5 nm, same as NH3 depth. Moreover, NH5 reveals an astonishing structure where the immense diamond-shaped hole is occupied by two QDs (Fig. 4.8(c)). The hole widths span 350 nm and 340 nm in the [1-10] and [110] directions, respectively, while the QD heights are about 4 nm, with respect to the hole bottom. Such diamond shape was reported in InAs/GaAs-QDs growth on a defect site via droplet epitaxy (Z.B. Cheng et al, 2013) [47]. They discovered that droplet prefer to form on detect sites, and one of the results shows diamond-shaped droplets forming on V-shaped defects, double-line defects pointing from the underlying substrate to the surface. The diamond-shape NHs also should be the results of high-strain dislocation, especially a line-defect TDs which provide high strain [48]. The large bottom area of NH5 compared with QDs, also, implies that the strain field should originate from the underlying layer.

Sample B. A 5 × 5 μm^2 AFM image in Fig 4.9(a) shows nanostructures around a [110] MD line where the areas labeled 1 and 2 are zoomed in and shown in Fig 4.9(b) and (c), respectively. In the same manner as sample A, the high-contrast color scales are applied to Fig 4.9(a) and 4.9(b) whereas the scale ranges are lowered to ~4.5 nm in order to discriminate the nanostructures mounds. The QD densities in box1 and box2 are different even on the same [110] MD line; the results reflect non-uniform strain field along the [110] MD line. The nanostructures on the [110] MD line can be divided into two cases, as follows. For the first case which is the *majority*, QDs are small and uniform whereas the mounds underneath vanish, or barely observed. For the second case which is the *minority*, big and non-uniform QDs are formed on the clearly-observed mounds. Also, the shapes of mounds are asymmetrical, similar to the NHs in sample A.

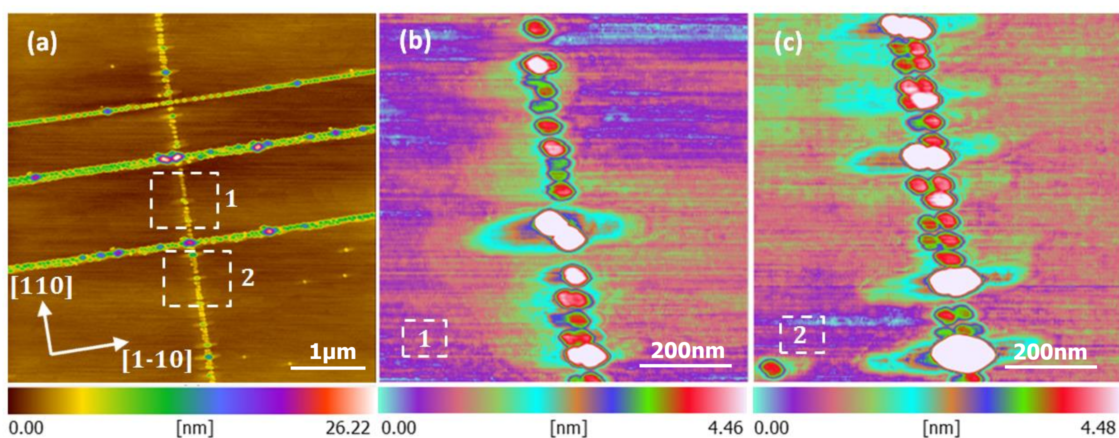

Figure 4.9 (a) 5 × 5 μm^2 AFM image at a [110] MD line of sample B. 800 × 800 nm^2 AFM images retrieved from (b) box1 and (c) box2.

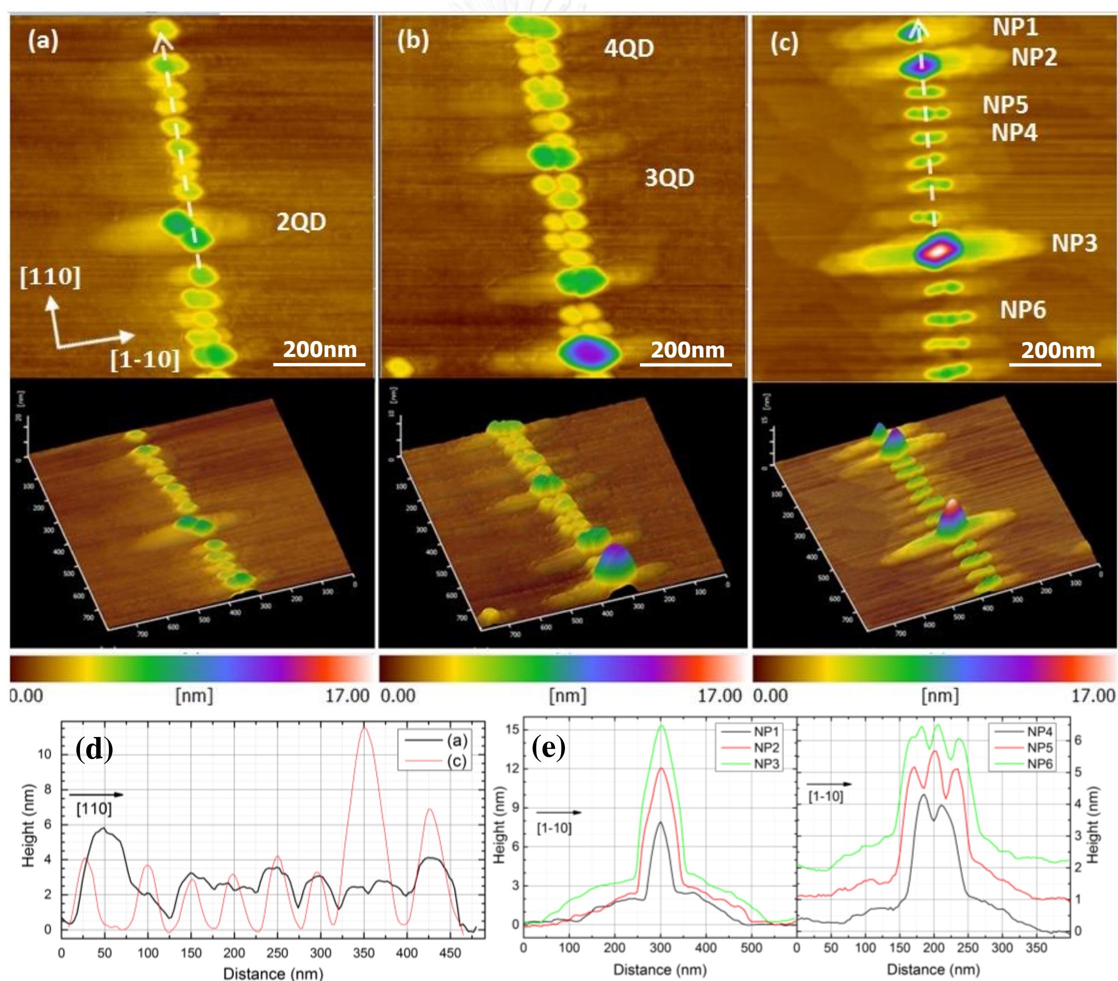

Figure 4.10 (a)-(c) 800 × 800 nm^2 AFM images and oblique 3D views at [110] MD lines of sample B. (d) Linescans in the [110] direction of QDs in figure 4.10 (a) and figure 4.10 (b). (e) Linescans in the [1-10] direction of NP1 to NP6.

For QD examination, the two AFM images are re-presented with appropriate scale colors and ranges in Figs. 4.10(a) and (b), including oblique 3D views. In addition, the surface morphology from another different location is investigated and shown Fig. 4.10(c). Linescans along the [110] direction corresponding to QDs in Figs. 4.10(a) and (c) are presented in Fig. 4.10(d) as well.

For QDs in Figs. 4.10(a) and (b), the average height of the *majority* QDs (yellow and light green color) is about 3 nm, while dark green QDs are 5.5-6.5 nm, and a purple QD is 12 nm. The number of QDs on a mound can vary between one and four. Interestingly, the shape of a 4-QDs-on-mound nanostructure (Fig. 4.10(b)) closely resembles the unit cell of a well-known quantum cellular automata (QCA), a building block for quantum computation. Close-up images of the four QDs on a mound and the schematic of QCA unit cells are shown in Fig. 4.11.

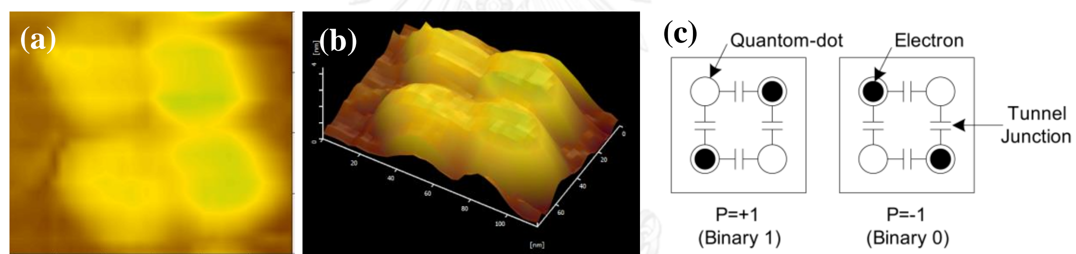

Figure 4.11 (a) 120 × 80 nm^2 AFM image and (b) oblique 3D view of a NP occupied by 4 QDs. (c) The schematic diagram of two QCA unit cells [49].

In contrast, the AFM image from the other location (Fig. 4.10(c)) exposes a clear observation in every mound, and surprisingly the shapes of QDs, as seen in the linescan (Fig. 4.10(d)), look fairly slender (like an inverse “V”), compared with the tubby QDs (like an inverse “U”) from the previous location. The causes of this deviation could be from differences in strain fields, growth rates, surface temperatures, or some other factors. Since every QD is, clearly, on a mound, the nanostructures will be called NPs in this thesis. The NPs can be separated into two cases, similar to the former location: firstly the *majority* with small and uniform QDs, and secondly the *minority* with big and non-uniform QDs.

The examples for the NP *majority* (NP4-NP6) and NP *minority* NPs (NP1-NP3) are selected from Fig. 4.10(c) and their linescans are shown in Fig 4.10 (e). For

the *majority*, the QD average height is 4.3 nm (green color). The number of QDs on a mound can vary from two (NP4) to three (NP5) and four (NP6). For the *minority*, the AFM image shows that the large-dimensional QDs (of NP1 to NP3) have *diamond bases*. This can be correlated with the diamond-shaped NHs in sample A. According to the linescans, the heights of the QDs increase from 6.5 nm (NP1) to 12 nm (NP2) and 15 nm (NP3), and the widths of the corresponding mounds broaden from 300 nm (NP1) to 400 nm (NP2) and 500 nm (NP3). Because the QD dimensions are associated with the strain, the larger the NH has the higher strain.

Sample C. The surface morphologies of two different locations are investigated. For the first location whose the surface morphology is shown in Figs. 4.12(a) and (b), it is expected to be a subsequent stage of the location where the slender QDs are found in sample B (Fig. 4.10(b)). The AFM image in Fig. 4.12 (a) shows asymmetric densities of the QDs locating along the two sides of a [110] MD line: the number of QDs on the left hand side is higher than that of the right hand side. This is the results of asymmetric MD stress, as discussed in the previous section. The magnifying AFM image in Fig 4.12(b) shows that the mounds on the left hand side tend to be larger than those on the right hand side. Due to the fact that InAs QDs are usually crowded on the preferential tensile areas (the left hand side), we can conclude that the mounds on the tensile side (the left hand side) tend to be larger than those on the compressive side (the right hand side), confirming the previous assumption regarding the NHs nucleation in sample A.

QDMs, comprising cQDs and sQDs, are observed in Fig. 4.12(b). However, there are certain NPs with any sQDs, or the sQDs are obscure. In this work, nanostructures are called QDMs when they fulfill two conditions: firstly the cQD sizes are significantly larger than the corresponding-sQD sizes, and secondly sQDs can be discriminated clearly. Therefore, the other QDs on the [110] MD lines, which are not QDMs, are called *normal QDs (nQDs).* Also, the large cQDs with diamond bases are called dQDs.

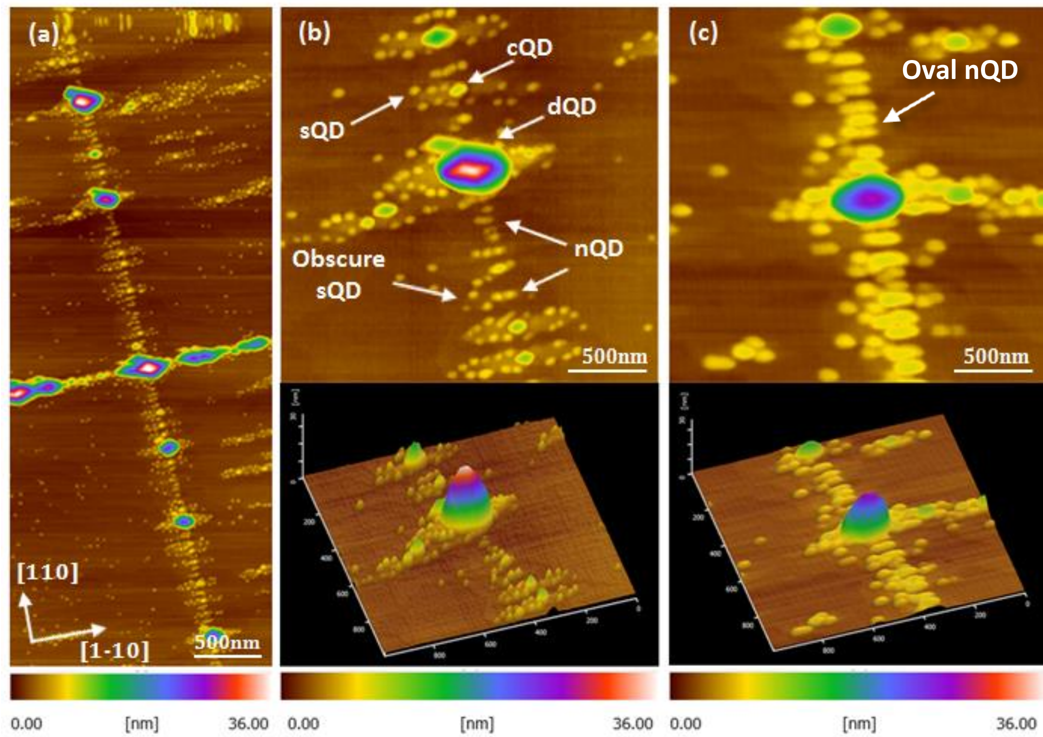

Figure 4.12 (a) A 2 × 5 μm^2 AFM image at a [110] MD line of sample C. (b and c) Close-up AFM images and oblique 3D views from two different locations.

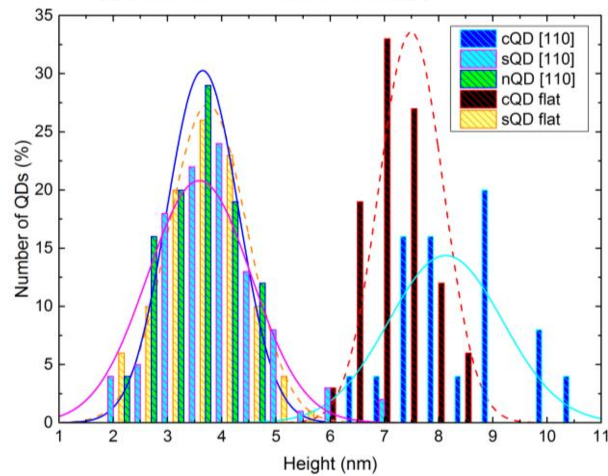

Figure 4.13 The height histogram of QDMs and nQDs (solid line) on a [110] MD line from figure 4.11(b) and QDMs (dash line) from a neraby flat area.

Fig. 4.13 shows the height histograms of QDs on [110] MD lines which are analyzed from the 2 × 5 μm^2 AFM in Fig. 4.12(a); also, the cQD and sQD histograms from nearby flat surfaces are shown as a reference. The dQDs with large dimensions (>15nm) are excluded from the histograms. The results show the broad distribution of cQDs on [110] MD with a mean height of 8 nm, slightly greater than cQDs on flat surfaces with a mean height of 7.5 nm. Surprisingly, nQDs and sQDs on [110] MD lines have similar heights to sQDs on flat surfaces: their mean heights are about 3.75 nm. This may derive from the fact that they all are InAs QDs that nucleate on InGaAs mounds. However, the distribution of sQDs on [110] MD line is slightly broader which reflects the influence of the asymmetric MD stress.

For the second location whose the surface morphology is shown in Fig. 4.12(c), it is expected to be a subsequent stage of the location where the tubby QDs are found in sample B (Fig. 4.10(b)). Four QD types—cQD, sQD, nQD, and dQD—are observed, but the shape of nQDs is oval, elongated in the [1-10] direction. The height of oval QDs is about 3 nm, whereas the widths in the two orthogonal directions are 115 and 40 nm. The existence of oval QDs was reported before in vertical stacked QDs grown on CHPs [44].

จุฬาลงกรณ์มหาวิทยาลัย
CHULALONGKORN UNIVERSITY

4.2.3 [1-10] MD lines

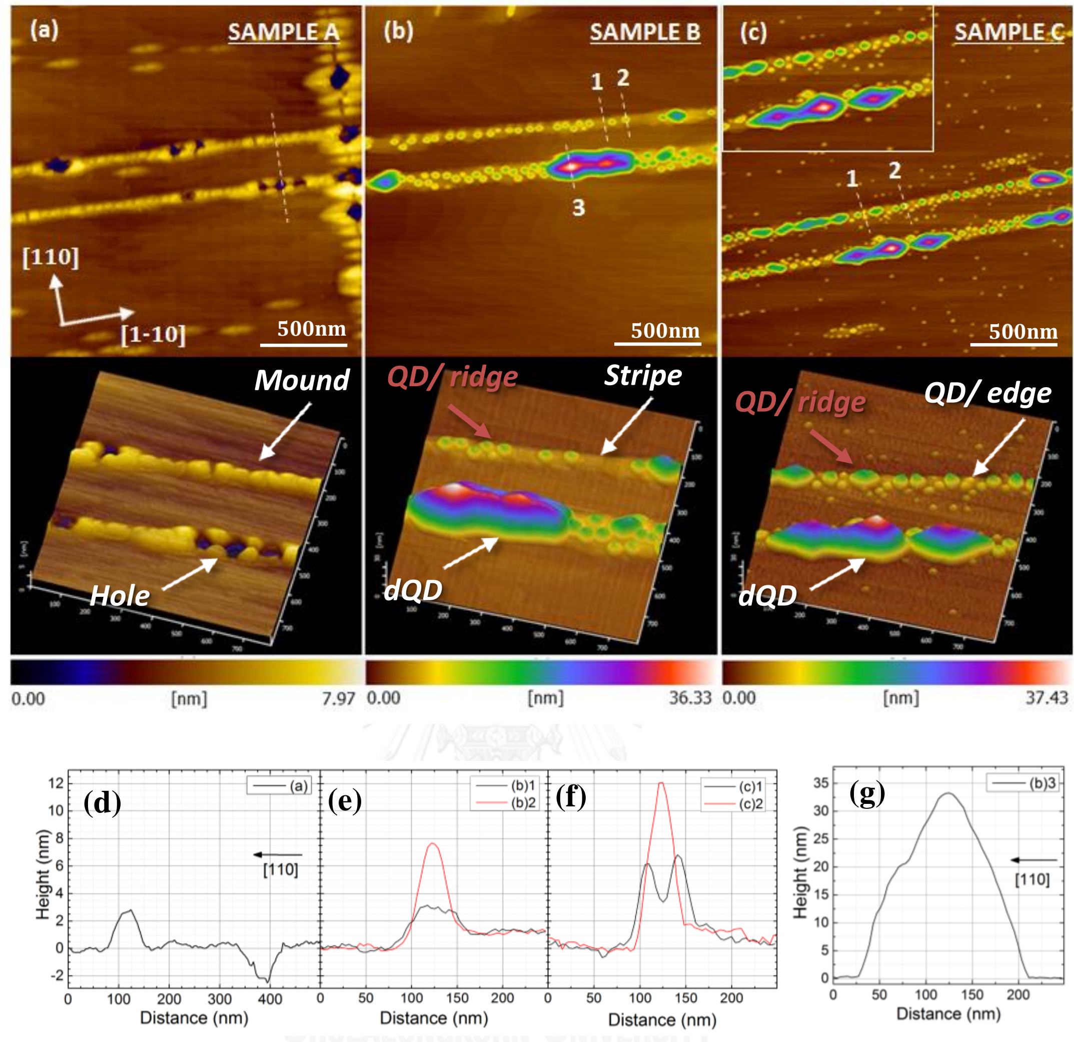

Figure 4.14 2×2 μm^2 AFM images and oblique 3D views at [110] MD lines of (a) sample A , (b) sample B, and (c) sample C. (d - g) Linescans in the [110] direction of the given lines of the three AFM images.

On [1-10] MD lines, the strain field is the highest; thus primary QD size and density are larger than those on the other areas. In contrast to [110] MD line, asymmetric MD stress should not affect the symmetry of nanostructures that elongated in the [1-10] direction: the stress along the [1-10] direction of a [1-10] MD is entirely uniform, according to the strain-field model discussed in section 4.1. The surface morphologies around [1-10] MD lines of the three samples are investigated and shown in the 2×2 μm^2 AFM images (upper parts) and oblique 3D images (lower parts) in Fig. 4.14.

Sample A. As shown in Fig 4.14 (a), the deposition of 10-ML GaAs has transformed most of the QDs into lower mounds attaching together and forming a stripe; yet a few NHs are observed on [1-10] MD lines. The linescan along the [110] direction in Fig. 4.14(d) shows the mound height of 3 nm, the NH depth of 2 nm below the flat surface.

The nucleation of a mound stripe can be explained as follows. During the early stage of GaAs capping, In atoms spread out from each QD in the [1-10] direction and QDs collapse as explained in the previous part. Because of the dense QD alignment along the [1-10] direction, In atoms cannot spread far and subsequently merge with those from nearby QDs, thus forming a stripe. However, holes on the mounds are not observed.

In the case of NHs, this is attributed to the high strain from [1-10] MD lines, similar to the case of diamond-shaped NHs on [110] MD lines that dig out the surface. It seems like the strain is so high that In atoms migrate out of the QD relatively fast, and also In atoms from nearby QDs do not prefer to move in the area either. Moreover, GaAs deposition rate on the high strain areas is relatively low, so the NHs are left on the surface.

Sample B. As shown in Fig 4.14 (b), the deposition of 1.0-ML InAs has transformed the mound stripes into smooth undulation surfaces on which QDs form. Most of the QDs (light green) located on the stripe's ridge are small and uniform; a few diamond-based QDs (dQDs) located on the NHs are distinctly large and non-uniform. The discovery of dQDs is the evidence that the deep NHs on [110] and [1-10] MD lines have similarly high strain field, and they act as In sinks.

The linescans along the [110] direction in Fig. 4.14(e) show a 1-nm height offset between the two sides of a stripe which should derive from the asymmetric stress of MDs: InAs prefer to deposite on the tensile side more than on the compressive side. The height of a stripe and a QD, with respect to the lower surface, are 3 nm and 8 nm, respectively. In contrast, the linescan of a dQD in Fig. 4.14 (g) shows the large height of 33 nm.

Sample C. As shown in Fig 4.14 (c), the deposition of 1.5-ML InAs has developed another group of QDs on the stipe's *edge* (yellow color), instead of the QDs on the strip's *ridge* (green color) and dQDs as found earlier in sample B. For this sample, QDs are categorized into three groups: (1) *eQD* for small QDs on strip's *edges*, (2) *rQD* for middle QDs on stripe's *ridges*, and (3) *dQD* for large *diamond-based* QDs on the NHs. It is interesting to note that if we consider the QD nucleation sequence and dimensions, the rQD and eQD on [1-10] MDs are analogous nanostructures for the cQD and sQD on flat surfaces, respectively.

Linescans along the [110] direction of an rQD and two eQDs are shown in Fig. 4.14(f). A 1-nm surface-height offset is observed, same as the case of sample B. The height of rQD is 9 nm, whereas the heights of two eQDs are 6 and 7 nm. In addition, the numbers of eQDs that are located on the two sides of [1-10] MDs lines are asymmetric: eQDs are crowded on higher-surface side compared with the lower-surface side. For example, the investigation on the upper [1-10] MD line in magnifying AFM image of Fig. 4.14(c) shows that there are 15 QDs on the higher-surface side and 3 QDs on the lower-surface side. This is the results of asymmetric MD stress: the higher-surface side has tensile stress, and the other side has compressive stress.

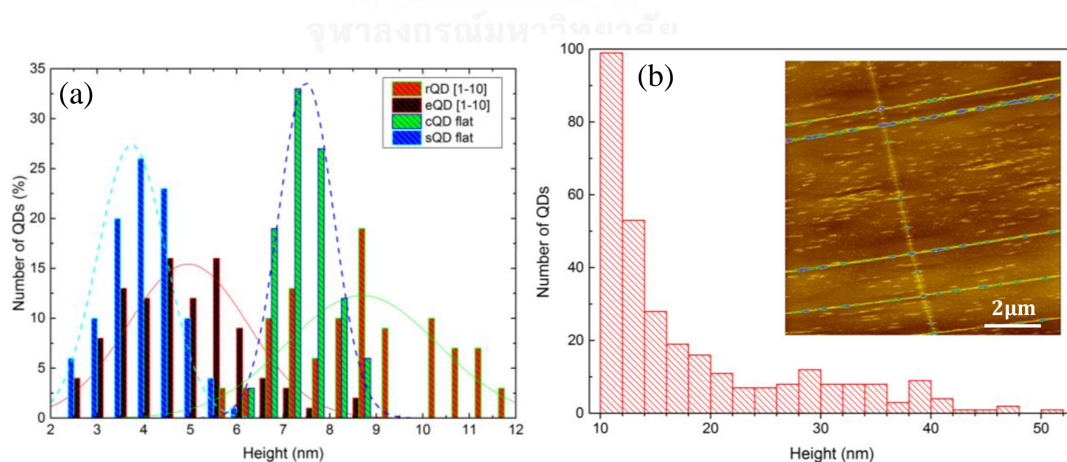

Figure 4.15 (a) Height histograms of rQDs and eQDs (solid line) on a [1-10] MD line from figure 4.14 (c) and QDMs, comprising cQDs and sQD (dash line), from a nearby flat surface. (b) 2 × 2 μm^2 AFM image and a corresponding dQD height histogram.

Fig. 4.15(a) shows the height histograms of rQDs and eQDs obtained from the $2 \times 2\ \mu m^2$ AFM image in Fig. 4.14(c). The histograms of cQDs and sQDs from the nearby flat surface are shown as a reference. The average heights of rQDs and eQDs are 9 nm and 5 nm, whereas the average heights of cQDs and sQDs are 7.5 and 4 nm, respectively. The results reflect the difference in the strains between [1-10] MDs and flat surfaces.

In the case of dQDs, the histogram taken from $10 \times 10\ \mu m^2$ AFM image is shown in fig. 4.15(b) where only QDs with the highs greater than 10 nm are calculated. The results show that most of the QDs fall in the 10-12 nm range, and then QD number drastically decrease to ~50 and 30 dots for the 12-14 nm and 14-16 nm ranges, respectively. The QD number remains steady at ~10 dots in the 20-36 nm range. The highest QD with 52 nm is found on the intersection.

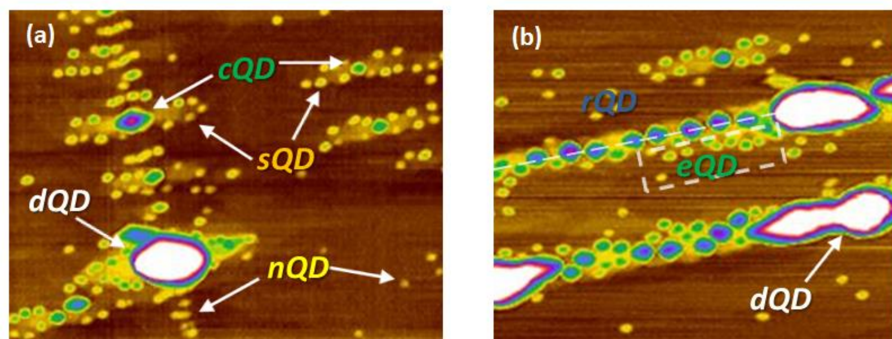

Figure 4.16 AFM images at (a) [110] and (b) [1-10] MD lines from sample C.

CHULALONGKORN UNIVERSITY

Table 4.3 The summary of QDs that are observed in sample C.

	Abbreviation	Full name	Nucleation sequence	Average height(nm)	FWHM (nm)
Flat surface	cQD	Center quantum dot	1	7.5	1.4
	sQD	Satellite quantum dot	2	3.75	1.7
	nQD	Normal quantum dot	2	3.55	1.6
[110] MD lines	dQD	Diamond-shaped quantum dot	1	-	-
	cQD	Center quantum dot	1	8.15	2.5
	sQD	Satellite quantum dot	2	3.65	2.3
	nQD	Normal quantum dot	2	3.60	1.6
[1-10] MD lines	dQD	Diamond-shaped quantum dot	1	-	-
	rQD	Ridge quantum dot	1	8.75	3.1
	eQD	Edge quantum dot	2	4.95	3.8

The last part of this section is dedicated to conclude the nanostructures on sample C, whose the optical properties will be investigated in the next. The details of QDs on the three different locations—flat areas, [110] MD lines, and [1-10] MD lines—are summarized in Tab. 4.3, and examples for ten QD types are shown in Fig. 4.16. The average heights and FWHM are calculated from QDs in the same locations for meaningful comparison. For the nucleation sequence, “1” is given to the QDs that nucleate sooner (in sample B), and “2” is given to the QDs that nucleate later (in sample C).

4.3 Optical properties of QDMs on CHPs

This section presents the photoluminescent (PL) results of QDM/CHP nanostructures. A sample with an identical structure to sample C is capped by 100-nm GaAs and undergone PL measurements according to the experimental setup explained in Chapter 3. This section is divided into two parts: the first reports the PL spectra of the sample subject to different excitation powers, whereas the second reports similar results under a fixed power but at different temperatures.

4.3.1 Power-dependent PL

In this experiment, the excitation power is varied from 10 mW to 230 mW whereas the sample temperature is maintained at 20K. The overall results show that at higher laser intensity the sample signals are also higher as a result of more electron-hole pairs. However, if the laser intensity is too high, it may cause saturation of some spectra peaks, and it may overheat or damage sample surface. The PL results in log scale are shown in Fig. 4.17.

จุฬาลงกรณ์มหาวิทยาลัย
Chulalongkorn University

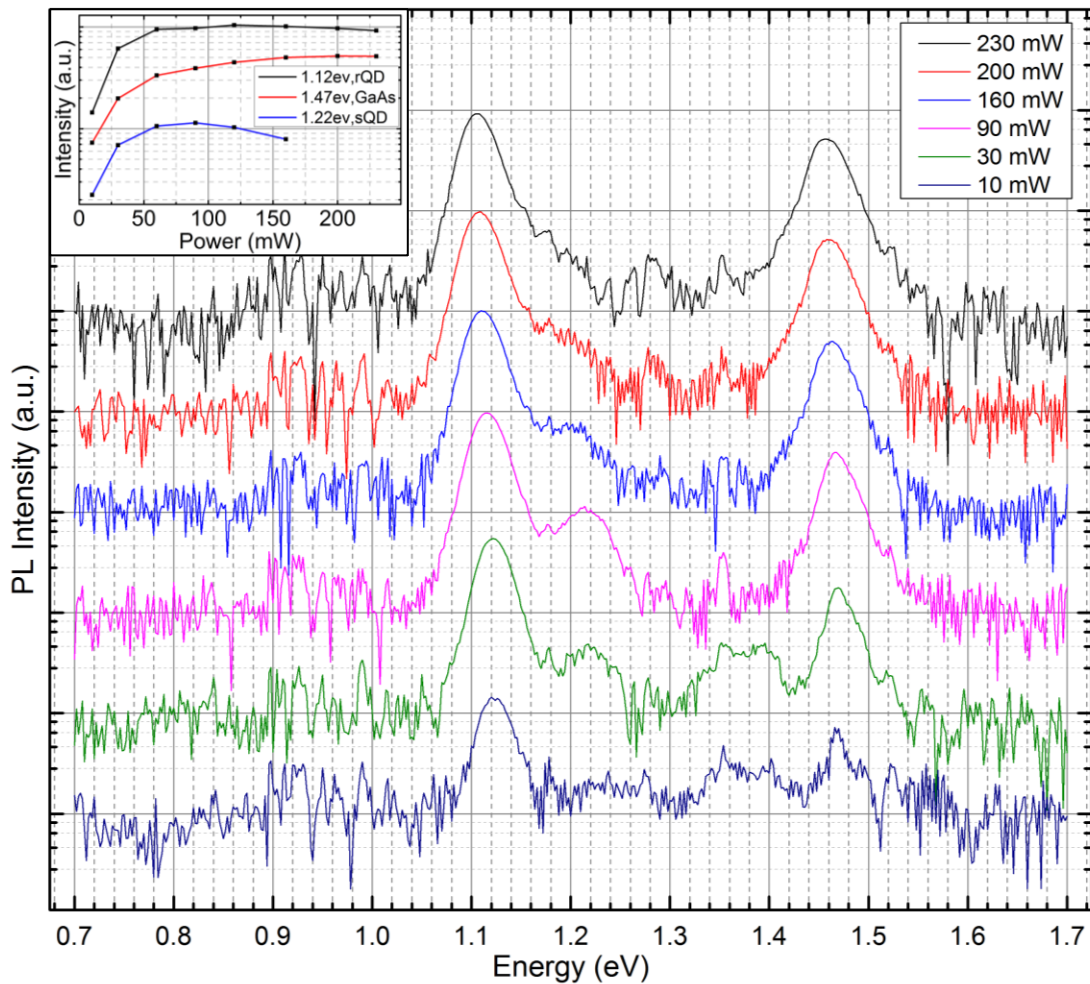

Figure 4.17 20-K PL spectra results of QDMs on CHPs measured in power-dependent experiment and accompany with a small inset of power-dependent peak intensity.

At low excitation power (10 mW), spectra with relatively high intensity are observed between the 0.89-1.6 eV range, and they are considered as sample signals. The three highest peaks are at 1.12 eV, 1.47 eV, and 1.35 eV, respectively. The first peak is emitted from QD nanostructures, whereas the last two peaks derive from GaAs buffer layer, with carbon contamination, and InAs wetting layer [44]. In addition, $In_{0.2}Ga_{0.8}As$ and GaAs-substrate peaks are observed at 1.27 eV [50] and 1.52 eV, respectively.

When the excitation power increases, the peaks of GaAs at 1.47 eV and QDs at 1.12 eV correspondingly increase. At 30 mW, another peak with high and broad spectrum is observed at 1.22 eV; however, the peak drop down after the excitation power of 90 mW. This should be a result of temperature variation since the red shifts of the peaks at 1.47 eV and 1.12 eV are observed for the high excitation power (90 – 230 mW). The PL intensity-temperature plots of the three peaks at 1.47 eV, 1.22 eV, and 1.12 eV are shown as the inset in Fig. 4.17.

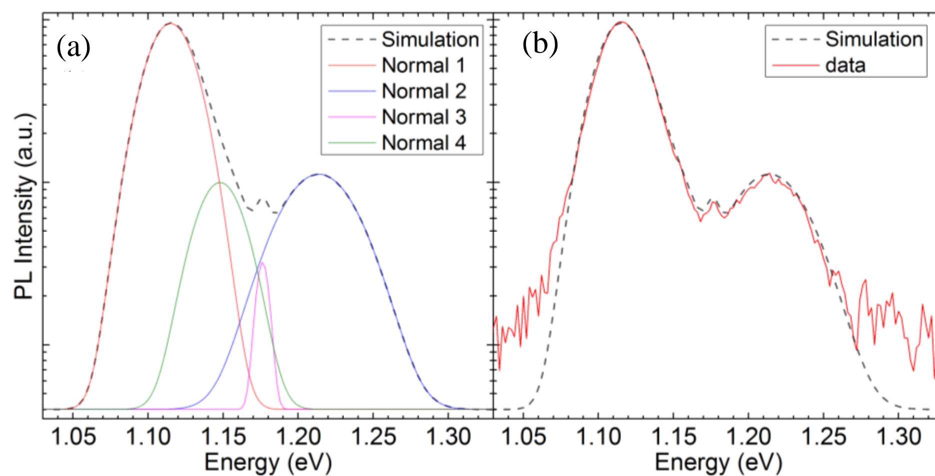

Figure 4.18 (a) Spectra simulated by Gaussian-fitting method. (b) A comparison between simulated and experimental spectra measured at 20 K and 90-mW excitation power.

The PL signals in 1.05-1.30 eV range are fitted by Gaussian functions, and the results are presented in Fig. 4.18. Four normal distributions can be resolved: their energy peaks are centered at 1.12 eV, 1.15 eV, 1.18 eV, and 1.21 eV; and the corresponding FWHM are 35 meV, 28 meV, 11 meV, and 52 meV, respectively. Based on (1) the quantum size effects that the bigger QD emits photons at the lower energy and (2) the FWHM of QD size distribution that relates to the PL FWHM, the spectra peaks can be used to describe the QDs as follows. If we consider from the uniform QD majority (excluding dQDs), the broad peak at 1.21 eV should be emitted from sQDs. Thus, the lower energy peaks at 1.18 eV, 1.15 eV, and 1.12 eV should be originated from eQD on [1-10] MDs, cQD on flat surfaces, and rQDs on [1-10] MDs, respectively.

At the highest excitation power (230 mW), there clearly exist two low-energy peaks at 1.24 eV and 1.26 eV, which should be emitted from small nQDs on [110] MD and flat surfaces, respectively. For the sharp peaks with energy lower than 1.12 eV, they should be emitted from large and non-uniform dQDs on [110] and [1-10] MD lines.

4.3.2 Temperature-dependent PL

In this experiment, the sample temperature is varied from 20 K to 120K, while the excitation power is maintained at 90 mW. Normally, when the temperature increases, the peaks of InAs QDs and GaAs should be red shifted due to Varshni law, and the spectra intensities should be lower due to thermal escape and non-radiative recombination. Fig. 4.19 shows the temperature-dependent PL results in log scale.

The results show clear red shifts in the peaks of GaAs (1.47 eV) and rQDs on [1-10] MDs (1.12 eV) when the temperature increases. The peak of sQDs (1.22 eV) drastically decreases and disappear when the temperature increase to 80 K. This is possible from the carrier migration from the small sQDs to large cQDs at high temperature [33]. At 100 K, the peak of cQD (1.17 eV) and eQDs (1.15 eV) on [110] MDs can be observed clearly. The peak intensity of rQDs (1.12 eV) decreases at a faster rate than that of GaAs (1.47 eV) and finally becomes lower when at 120K. The fast decrease in the rQD peak, compared to bulk GaAs, should derive from carrier migration from the small rQDs to the large dQDs on [1-10] MDs. Moreover, the peaks of cQDs (1.17 eV) and large dQDs (< 1.12 eV) remain even at high temperature (120K).

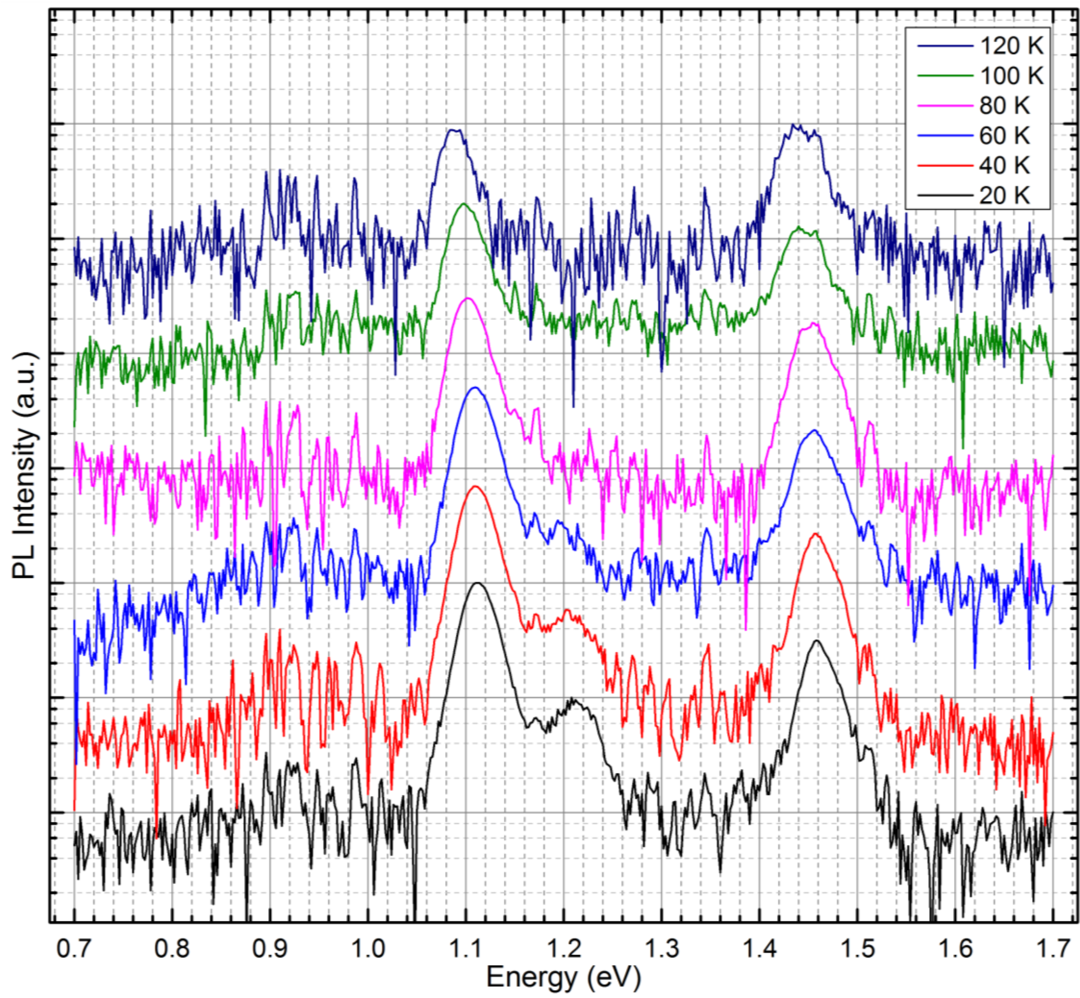

จุฬาลงกรณ์มหาวิทยาลัย
Chulalongkorn University

Figure 4.19 PL spectra results of QDMs on CHPs measured in temperature-dependent experiment at 90-mW excitation power.

CHAPTER 5
Conclusions

This thesis studies the evolution and characteristics of quantum dot molecules (QDMs) on cross hatch patterns (CHPs). To study the evolution of QDMs, a series of three samples (A, B, and C) was fabricated on identical $In_{0.2}Ga_{0.8}As$-CHP virtual substrates, and the surface morphologies were studied by atomic force microscopy (AFM). Sample A is nanoholes (NHs) grown by the deposition of 10-ML GaAs on 1.7-ML InAs QDs. Sample B is nanopropellers (NPs) grown by the deposition of 1.0-ML InAs on the NHs. Sample C is QDMs grown by the deposition of 1.5-ML InAs on the NHs. Also, the optical properties of QDMs on CHPs (Sample C) were studied by photoluminescence (PL).

On CHPs, the nanostructures of the three samples show high variations which can be considered in three different locations:

1. **Flat surfaces**. For samples A and B, the nanostructures are NHs and NPs, respectively, which are uniform and similar to those grown on flat GaAs substrates in the previous works. For Sample C, the nanostructures are QDMs and normal QDs (nQDs). The fact that nQDs occur, despite the In deposition (1.5 ML) is lower than the critical thickness (1.7 ML), indicates the effects of accumulated strain from the underlying InAs wetting layer and the CHPs. The QD sizes in ascending order are 3.6 nm for nQDs, 3.8 nm for satellite QDs (sQDs), and 7.5 nm for center QDs (cQDs).

2. **[110] MD lines**. For sample A, the nanostructures are asymmetric NHs due to asymmetric stress of MDs: mounds on the tensile areas tend to be larger than mounds on the compressive areas. The MD strain enlarges certain NHs: the mound and hole sizes increase as a result of the conservation of mass. Large NHs have diamond shapes, and QDs in the bottom of very large NHs are observed.

For Sample B, the nanostructures are NPs, and the number of QDs per NP ranges from 1 to 4 dots. The NP which resembles the unit cell of quantum cellular automata (QCA) is recognized. The mounds of certain NPs are obscure. Diamond-based QDs (dQDs) of large NPs are observed; this can be correlated with the diamond-shaped NHs in Sample A. The investigation from two different locations

shows the variation in shapes of QDs: slender QDs (like an inverse "V") and tubby QDs (like an inverse "U").

For Sample C, the nanostructures are QDMs and nQDs. The numbers of sQDs in the two sides of MD lines are asymmetric due to asymmetric MD stress. Certain sQD are obscure. Large cQDs have diamond shapes. The shapes of nQDs from certain locations are oval, with elongation axis along [1-10] direction. The average size of cQDs is the largest at 8.2 nm, whereas the average sizes of sQDs and nQDs are similar at 3.6 nm.

3. **[1-10] MD lines**. For Sample A, the nanostructures are NHs which are deeper than the surface and mounds which align closely along the [1-10] direction. Holes are not observed on the mounds.

For Sample B, the nanostructures are large dQDs on the NHs, and rQDs on the stripe's ridge. The stripes are smooth undulation surfaces which develop from the mound strip in Sample A. There is a 1-nm height offset between the two sides of a stripe due to the asymmetric stress of MDs.

For Sample C, the nanostructures are dQDs, rQDs, and another type of QDs which nucleate on the strip's edge (called eQDs). The height offset between the two sides of the stripe is observed, and eQDs prefer to from on the higher sides (tensile areas) rather than the lower sides (compressive areas). The QD sizes are 4.95 nm for eQDs and 8.75 nm for rQDs.

The power-dependent PL experiment at 20 K shows that Sample C emits broad signals from 0.89-1.6 eV. The important peaks are from GaAs (1.47 eV), InAs wetting layer (1.35 eV), $In_{0.2}Ga_{0.8}As$ CHP (1.27 eV), nQDs on flat surfaces (1.26 eV), nQDs on [110] MD (1.24 eV), sQDs on flats surface and [110] MD (1.21 eV), cQDs on flat surface (1.18 eV), eQDs (1.15 eV), rQDs (1.18 eV), and dQDs (<1.02eV).

The temperature-dependent PL experiment shows clear red shifts in the peaks of GaAs and rQDs. The peak of sQDs disappears at 80 K due to carrier migration from small sQDs to large cQDs at high temperatures. Also, the fast decrease in the rQD peak intensity is attributed to the carrier migration from small rQDs to large dQDs on [1-10] MD lines.

REFERENCES

1. Madureira, N.L., *Oil Reserves and Peak Oil*, in *Key Concepts in Energy*. 2014, Springer International Publishing: Cham. p. 101-130.
2. Tiedje, T., et al., *Limiting efficiency of silicon solar cells.* IEEE Transactions on Electron Devices, 1984. **31**(5): p. 711-716.
3. Hanna, M.C., Z. Lu, and A.J. Nozik, *Hot carrier solar cells.* AIP Conference Proceedings, 1997. **404**(1): p. 309-316.
4. Würfel, P., *Solar energy conversion with hot electrons from impact ionisation.* Solar Energy Materials and Solar Cells, 1997. **46**(1): p. 43-52.
5. Yablonovitch, E., O.D. Miller, and S.R. Kurtz. *The opto-electronic physics that broke the efficiency limit in solar cells*. in *Photovoltaic Specialists Conference (PVSC), 2012 38th IEEE*. 2012.
6. Dimroth, F., et al., *Wafer bonded four-junction GaInP/GaAs//GaInAsP/GaInAs concentrator solar cells with 44.7% efficiency.* Progress in Photovoltaics: Research and Applications, 2014. **22**(3): p. 277-282.
7. Nozawa, T. and Y. Arakawa, *Detailed balance limit of the efficiency of multilevel intermediate band solar cells.* Applied Physics Letters, 2011. **98**(17): p. 171108.
8. National Renewable Energy Laboratory. *Research Cell Efficiency Records*. 2016 February 25, 2016 [cited 2016 April 25]; Available from: http://www.nrel.gov/ncpv/images/efficiency_chart.jpg.
9. Jenks, S. and R. Gilmore, *Material Selection for the Quantum Dot Intermediate Band Solar Cell*, in *Quantum Dot Solar Cells*, J. Wu and M.Z. Wang, Editors. 2014, Springer New York: New York, NY. p. 135-166.
10. Rostami, A., K. Abbasian, and N. Gorji, *Efficiency optimization in a rainbow quantum dot solar cell.* International Journal on Technical and Physical Problems of Engineering, 2011. **3**(7): p. 106-109.
11. Limwongse, T., et al., *InGaAs Quantum Dots on Cross-Hatch Patterns as a Host for Diluted Magnetic Semiconductor Medium.* Journal of Nanomaterials, 2013. **2013**: p. 1-5.
12. Suraprapapich, S., et al., *Self-assembled quantum-dot molecules by molecular-beam epitaxy.* Journal of Vacuum Science & Technology B: Microelectronics and Nanometer Structures, 2005. **23**(3): p. 1217.
13. Jevasuwan, W., S. Ratanathammapan, and S. Panyakeow, *InP Ring-Shaped Quantum Dot Molecules by Droplet Epitaxy*, in *Quantum Dot Molecules*, J. Wu and M.Z. Wang, Editors. 2014, Springer New York: New York, NY. p. 29-49.
14. Vorathamrong, S., et al., *Effect of Ga Pre-Deposition Rate on GaAs Nanowires Grown by Self-Assisted VLS Method Using MBE on SiO2/Si(111) Substrates.* Advanced Materials Research, 2016. **1131**: p. 12-15.
15. Patanasemakul, N., S. Panyakeow, and S. Kanjanachuchai, *Chirped InGaAs quantum dot molecules for broadband applications.* Nanoscale Research Letters, 2012. **7**(1): p. 1-9.

16. Himwas, C., S. Panyakeow, and S. Kanjanachuchai, *Optical properties of as-grown and annealed InAs quantum dots on InGaAs cross-hatch patterns.* Nanoscale Research Letters, 2011. **6**(1): p. 1-7.
17. Evan, D.R. *Notes for Microelectronic Device Fabrication I.* 2016 [cited 2016 April 25]; Available from: http://web.pdx.edu/~davide/notes.pdf.
18. Jasim, K.E., *Quantum Dots Solar Cells*, in *Solar Cells - New Approaches and Reviews*, L.A. Kosyachenko, Editor. 2015, InTech.
19. Eriksson, M.A., S.N. Coppersmith, and M.G. Lagally, *Semiconductor quantum dot qubits.* MRS Bulletin, 2013. **38**(10): p. 794-801.
20. Silva, G.A., *Neuroscience nanotechnology: progress, opportunities and challenges.* Nat Rev Neurosci, 2006. **7**(1): p. 65-74.
21. Kiravittaya, S., *Homogeneity improvement of InAs/GaAs self-assembled quantum dots grown by molecular beam epitaxy*, in *Faculty of Engineering*. 2002, Chulalongkorn University.
22. Daruka, I. and A.-L. Barabási, *Dislocation-Free Island Formation in Heteroepitaxial Growth: A Study at Equilibrium.* Physical Review Letters, 1997. **79**(19): p. 3708-3711.
23. Institut für Halbleiteroptik und Funktionelle Grenzflächen. *Lens-shaped Semiconductor Quantum Dot (Model).* 2014 [cited 2016 April 26]; Available from: https://www.yumpu.com/en/document/view/22556986/lens-shaped-semiconductor-quantum-dot-model.
24. Seifert, W., et al., *In-situ growth of quantum dot structures by the Stranski-Krastanow growth mode.* Progress in Crystal Growth and Characterization of Materials, 1996. **33**(4): p. 423-471.
25. Songmuang, R., *Study on growth and in-situ processing of InAs self-organized quantum dots for long wavelength applications*, in *Faculty of Engineering*. 2003, Chulalongkorn University.
26. Thudsalingkarnsakul, N., *Effective one-dimensional electronic structure of InGaAs quantum dot molecules*, in *Faculty of Engineering*. 2008, Chulalongkorn University.
27. Suraprapapich, S., et al., *Regrowth of self-assembled InAs quantum dots on nanohole and stripe templates.* Journal of Micro/Nanolithography, MEMS, and MOEMS, 2006. **5**(1): p. 011008-011008-5.
28. Suraprapapich, S., et al., *Thin-capping-and-regrowth molecular beam epitaxial technique for quantum dots and quantum-dot molecules.* Journal of Vacuum Science & Technology B, 2006. **24**(3): p. 1665-1667.
29. Kiravittaya, S., et al., *Multi-scale ordering of self-assembled InAs/GaAs(001) quantum dots.* Nanoscale Research Letters, 2006. **1**(1): p. 1-10.
30. Songmuang, R., S. Kiravittaya, and O.G. Schmidt, *Shape evolution of InAs quantum dots during overgrowth.* Journal of Crystal Growth, 2003. **249**(3–4): p. 416-421.
31. Costantini, G., et al., *Interplay between thermodynamics and kinetics in the capping of InAs/GaAs(001) quantum dots.* Phys Rev Lett, 2006. **96**(22): p. 226106.
32. Suraprapapich, S., *Self-assembled quantum dot molecules by molecular beam epitaxy and their potential applications*, in *Faculty of Engineering*. 2006, Chulalongkorn University.

33. Patanasemakul, N., *Optical emission from InAs quantum dot molecules*, in *Faculty of Engineering*. 2011, Chulalongkorn University.
34. Lee, J., et al., *Evolution of Various Nanostructures and Preservation of Self-Assembled InAs Quantum Dots During GaAs Capping.* IEEE Transactions on Nanotechnology, 2010. **9**(2): p. 149-156.
35. Siripitakchai, N., *Control of the number of dots in InAs quantum dot molecules for quantum computing*, in *Faculty of Engineering*. 2006, Chulalongkorn University.
36. Suraprapapich, S., et al., *Self-assembled lateral InAs quantum dot molecules: Dot ensemble control and polarization-dependent photoluminescence.* Microelectronic Engineering, 2006. **83**(4–9): p. 1526-1529.
37. Trisna, B.A., *RELIABLE SYNTHESIS AND MANIPULATION OF SELF-RUNNING GALLIUM DROPLETS ON GALLIUM ARSENIDE (001) IN MBE*, in *Faculty of Engineering*. 2014, Chulalongkorn University.
38. Farrell, H.H. and C.J. Palmstro/m, *Reflection high energy electron diffraction characteristic absences in GaAs(100) (2×4)–As: A tool for determining the surface stoichiometry.* Journal of Vacuum Science & Technology B, 1990. **8**(4): p. 903-907.
39. Panish, M.B. and H. Temkin, *Molecular Beam Epitaxy Systems and Procedures*, in *Gas Source Molecular Beam Epitaxy: Growth and Properties of Phosphorus Containing III-V Heterostructures*. 1993, Springer Berlin Heidelberg: Berlin, Heidelberg. p. 78-117.
40. Neave, J.H., et al., *Dynamics of film growth of GaAs by MBE from Rheed observations.* Applied Physics A. **31**(1): p. 1-8.
41. UPPSALA UNIVERSITET. *Atomic force microscopy (AFM)*. 2016 [cited 2016 April 26]; Available from: http://www.farmfak.uu.se/farm/farmfyskem/instrumentation/afm.html.
42. Heiman, D. *Photoluminescence Spectroscopy*. 2004 [cited 2016 April 27]; Available from: http://tns.ndhu.edu.tw/~clcheng/class-94/bio-phy94/Class-2-PL.pdf.
43. Chokamnuai, T., *Polarized photoluminescence of vertically stacked InAs quantum dots on cross-hatch patterns*, in *Faculty of Engineering*. 2013, Chulalongkorn University.
44. Jittrong, A., *The effects of reduced spacer thickness towards polarized photoluminescence of multi-stack InAs quantum dots on cross-hatch patterns*, in *Faculty of Engineering*. 2014, Chulalongkorn Univeristy.
45. Limwongse, T., *Evolution of InAs quantum dots grown on cross-hatch substrates*, in *Faculty of Engineering*. 2008, Chulalongkorn University.
46. Limwongse, T., S. Panyakeow, and S. Kanjanachuchai, *Evolution of InAs quantum dots grown on cross-hatch substrates.* physica status solidi (c), 2009. **6**(4): p. 806-809.
47. Chen, Z.B., et al., *Preferential nucleation and growth of InAs/GaAs(001) quantum dots on defected sites by droplet epitaxy.* Scripta Materialia, 2013. **69**(8): p. 638-641.
48. Kanjanachuchai, S. and T. Limwongse, *Nucleation Sequence of InAs Quantum Dots on Cross-Hatch Patterns.* Journal of Nanoscience and Nanotechnology, 2011. **11**(12): p. 10787-10791.

49. Cho, H. and J. E. E. Swartzlander, *Adder and Multiplier Design in Quantum-Dot Cellular Automata.* IEEE Transactions on Computers, 2009. **58**(6): p. 721-727.
50. Thet, C.C., S. Kanjanachuchai, and S. Panyakeow. *The Effects of Substrate Mounds and Pits on the Periodicity of Cross-Hatch Surface and Subsequent Formation of Quantum Dots*. in *2007 2nd IEEE International Conference on Nano/Micro Engineered and Molecular Systems*. 2007.

APPENDIX

จุฬาลงกรณ์มหาวิทยาลัย
Chulalongkorn University

VITA

Nitas Nakareseisoon was born in Bangkok, Thailand on March 17, 1990. He entered Chulalongkorn University and received the Bachelor of Engineering in Electrical Engineering with GPAX 3.52 in April 2013.

He entered the Graduate School of Chulalongkorn University in June 2013, as a Master Degree student in Semiconductor Research Devices Laboratory (SDRL), in the Department of Electrical Engineering, Faculty of Engineering.